



Postliquefaction Reconsolidation Settlement of a Soil Deposit Considering Spatially Variable Properties and Ground Motion Variability

Devdeep Basu¹; Jack Montgomery, Ph.D., P.E., M.ASCE²; and Armin W. Stuedlein, Ph.D., P.E., F.ASCE³

Abstract: Assessment of earthquake-induced liquefaction is an important topic in geotechnical engineering due to the significant potential for damage to infrastructure. Some of the most significant infrastructure damage occurs due to differential settlement of the ground, including due to liquefaction. Postliquefaction deformations commonly are assessed using one-dimensional empirical models, which inherently assume laterally homogeneous soil layers. Numerical models offer the potential to examine the effects of ground motion variability and spatially variable soil properties on liquefaction-induced deformations. This study explored the postliquefaction reconsolidation settlement for a site in Hollywood, South Carolina, which was characterized using a three-dimensional (3D) geostatistical model and simulated using the numerical platform FLAC and constitutive model PM4Sand. The effects of ground motion characteristics on mean and maximum differential settlements were investigated. The physical mechanisms associated with postliquefaction responses such as excess pore pressures, shear strains, and volumetric strains also were examined. The efficacy of uniform models assuming representative percentile soil properties to represent the stochastic mean settlement was investigated. The inherent inability of uniform models to capture differential settlements and therefore the need for using stochastic models is discussed. DOI: 10.1061/JGGEFK.GTENG-11768. © 2024 American Society of Civil Engineers.

Author keywords: Liquefaction; Numerical modeling; Spatial variability; Settlement.

Introduction

Dynamic loading during earthquakes can generate sufficient shear strain to generate excess pore pressures associated with liquefaction of granular soils. Settlement of the ground surface can occur both during and following liquefaction as volumetric strains accumulate within the liquefied layer and liquefied materials breach the ground surface as ejecta. Such settlements rarely are uniform, and differential settlement can cause significant damage to both underground (e.g., foundations and buried utilities) and surface infrastructure (e.g., buildings and bridges). Several empirical models have been developed to predict postliquefaction settlements using results from laboratory experiments and field observations (Tokimatsu and Seed 1987; Ishihara and Yoshimine 1992; Sento et al. 2004; Yoshimine et al. 2006; Idriss and Boulanger 2008). These models commonly estimate potential postliquefaction volumetric strains using profiles of penetration resistances from standard penetration tests (SPTs) or cone penetration tests (CPTs) and estimates of shear strain during earthquake loading. Several limitations in these empirical models or their use in practice have been highlighted, including

Note. This manuscript was submitted on March 16, 2023; approved on October 17, 2023; published online on January 3, 2024. Discussion period open until June 3, 2024; separate discussions must be submitted for individual papers. This paper is part of the *Journal of Geotechnical and Geoenvironmental Engineering*, © ASCE, ISSN 1090-0241.

overestimation of settlement for saturated soil layers that do not reach initial liquefaction (Geyin and Maurer 2019), neglecting effects of partial saturation or partial drainage (Banister et al. 1976), thin layers (Yost et al. 2019; Beyzaei et al. 2020; Cary et al. 2022), nonliquefiable crusts (Youd and Garris 1995; Green et al. 2018), and soil fabric (Lewis et al. 2008; Bwambale and Andrus 2019). These models also assume one-dimensional (1D) conditions, implying that the soil is laterally homogeneous. Most soil deposits are heterogeneous, with the properties varying spatially in both vertical and lateral directions. The effects of this spatial variability on liquefaction-induced differential settlements are not well understood.

Inherent spatial variability in soils generally arises from (1) variability in the thickness of a given soil layer (Fenton and Vanmarcke 1998), (2) variability in the lateral extent of a given soil layer (Lumb 1975), (3) the inherent variability in properties within a given layer (Phoon and Kulhawy 1999; Stuedlein and Bong 2017), and/or (4) a combination of all these sources. Although the variability arising from Sources 1 and 2 can be estimated reasonably using a sufficient number of soil explorations, the inherent variability (Source 3) in a soil stratum can never be fully quantified using any number of cost-effective explorations (Stuedlein and Bong 2017). Several in situ field tests and analytical studies have been carried out to improve the familiarity with inherent spatial variability and quantify it for geosystems (DeGroot and Baecher 1993; Phoon and Kulhawy 1999; Griffiths et al. 2002; Bong and Stuedlein 2017)

Spatial variability in soil deposits can cause significant differential settlements over a loaded area, leading to structural damage (Polshin and Tokar 1957). Popescu et al. (1997) used finite-element analyses to investigate the effect of spatial variability on excess pore pressures and displacements, and assessed the equivalent percentile deterministic properties that approximately matched the stochastic responses. Chen et al. (2016) developed a CPT-based

¹Postdoctoral Research Fellow, Dept. of Civil Engineering, Univ. of British Columbia, Vancouver, BC, Canada V6T 1Z4 (corresponding author). Email: devdeep.basu@ubc.ca

²Associate Professor, Dept. of Civil and Environmental Engineering, Auburn Univ., Auburn, AL 36849. ORCID: https://orcid.org/0000-0001-6501-7581

³Professor, School of Civil and Construction Engineering, Oregon State Univ., Corvallis, OR 97331. ORCID: https://orcid.org/0000-0002-6265

liquefaction model for the probabilistic and spatial assessment of liquefaction-induced settlements at the regional and surficial geologic unit scale as well as the local site-specific scale. Montgomery and Boulanger (2017) evaluated the effect of spatial variability on liquefaction-induced settlement and lateral spreading for gently sloping ground utilizing numerical modeling, and also recommended an equivalent percentile of uniform properties that can be used to approximate the stochastic behavior. Bong and Stuedlein (2018) used 1D liquefaction triggering and reconsolidation settlement analyses from a well-characterized test site to illustrate the role of spatial variability of overburden stress and clean sand-corrected cone tip resistance on the spatial distribution of differential settlement, and noted that lower shaking intensities may result in larger differential settlements than do high intensities. However, excess pore-pressure migration and the in-shaking system response (e.g., Cubrinovski et al. 2019) were not considered in these simplified analyses. Additional work is needed to understand the magnitude of differential settlement possible within spatially variable soil deposits and to compare numerical results with observations at field sites at which spatial variability in properties has been quantified.

Stuedlein et al. (2021) quantified the spatial variability in differential settlement following controlled blasting of displacement pile-improved ground using random field theory. They observed that whereas the autocorrelation length of reconsolidation settlement could be well-approximated by predensification corrected cone tip resistance (q_t) , soil behavior type index (I_c) , and fines content (FC), only the coefficient of inherent variability (COV_w) of silty fines appeared to be similar to the COV_w of settlement. Additionally, Stuedlein et al. (2021) showed that the predensification mean I_c and FC at specific locations was positively correlated with the magnitude of reconsolidation settlement, whereas no significant correlation to postdensification q_t , overburden stress and clean sand-corrected cone tip resistance (q_{c1Ncs}) , or relative density (D_r) was identified. Together, these findings suggest that the increased compressibility of silty fines constitutes the main variable driving the postdensification settlement expressed at the ground surface following dissipation of excess pore pressures. However, there are few sites at which liquefaction has been observed and soil properties have been quantified to a sufficiently high degree to enable stochastic modeling.

In this paper, numerical models were used to simulate the response of two-dimensional (2D) cross sections of a well-characterized site in Hollywood, South Carolina, that was subjected to blast-induced liquefaction. Numerous CPTs, downhole shear wave velocity tests, and mud-rotary borings had been performed at the site previously (Stuedlein et al. 2016; Gianella and Stuedlein 2017). This extensive characterization program provided good estimates of q_{c1Ncs} at the site, examined by Bong and Stuedlein (2017, 2018) to estimate the spatial variability of silty fines and

the magnitude of liquefaction-induced reconsolidation settlement that would be expected at the site using empirical models as described previously. This paper builds on this prior work using numerical simulations with the constitutive model PM4Sand v3.1 (Boulanger and Ziotopoulou 2017) and the finite-difference program FLAC v8.0. Numerical simulations used in this study incorporated spatially variable soil properties such as D_r and shear modulus based on correlations with q_{c1Ncs} . Uniform soil sections, using the median and percentiles from the q_{c1Ncs} distribution for the stochastic deposit, also were simulated to determine their ability to estimate the reconsolidation settlements computed in the stochastic models. Both synthetic, pseudo-harmonic earthquake loadings and a suite of recorded earthquake loadings were used as input motions to represent the expected seismic hazard at the Hollywood site. The effects of lateral boundary conditions on mean reconsolidation settlements and maximum differential settlements were investigated, and were found to influence significantly both the mean and maximum differential settlement if the boundaries were close to the region of interest (ROI). The effects of spatial variability on postliquefaction responses such as excess pore pressures, shear strain (γ) , and volumetric strain (ε_v) with q_{c1Ncs} and input motion parameters were examined. Comparisons with equivalent uniform models showed that using median soil properties reasonably captured the mean stochastic settlements, but not the maximum differential settlements, which are driven in part by ground motion variability and their evolutionary intensity measures.

Description of the Hollywood Test Site

The test site considered in this study is located in Hollywood, South Carolina, 20 km west of Charleston, and is set within the Lower Coastal Plain Unit formed during alternating periods of marine and fluvial deposition (Doar and Kendall 2014). The native beach sands are Pleistocene age deposits ranging from 70,000 to 200,000 years old (Maybin and Nystrom 1997; Andrus et al. 2008). This site previously was used to evaluate liquefaction mitigation using driven displacement piles through controlled blasting techniques (Stuedlein et al. 2016; Gianella and Stuedlein 2017). The site also has been used to examine the effects of pile spacing and installation on driving and penetration resistance (Stuedlein and Gianella 2016), time-dependent regain of small-strain stiffness (Mahvelati et al. 2016; Mahvelati et al. 2020), spatial variability of silty fines (Bong and Stuedlein 2017), and liquefaction-induced settlements (Bong and Stuedlein 2018; Stuedlein et al. 2021). The site has been characterized extensively using static and seismic CPTs, downhole- and surface wave-based shear wave velocity tests, and mud-rotary borings with split-spoon samples. Fig. 1 presents a plan view of the test site showing the locations of the initial 25 CPTs conducted in May 2014 and mud-rotary boreholes advanced in June 2014 to identify baseline subsurface conditions prior to

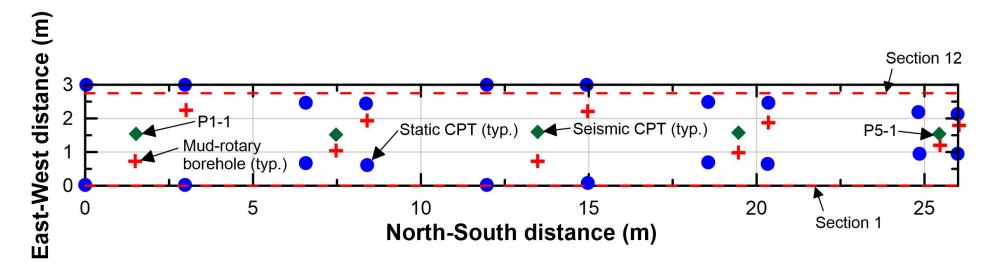


Fig. 1. Plan view of the Hollywood test site showing the locations of the various explorations performed. (Adapted from Bong and Stuedlein 2018.)

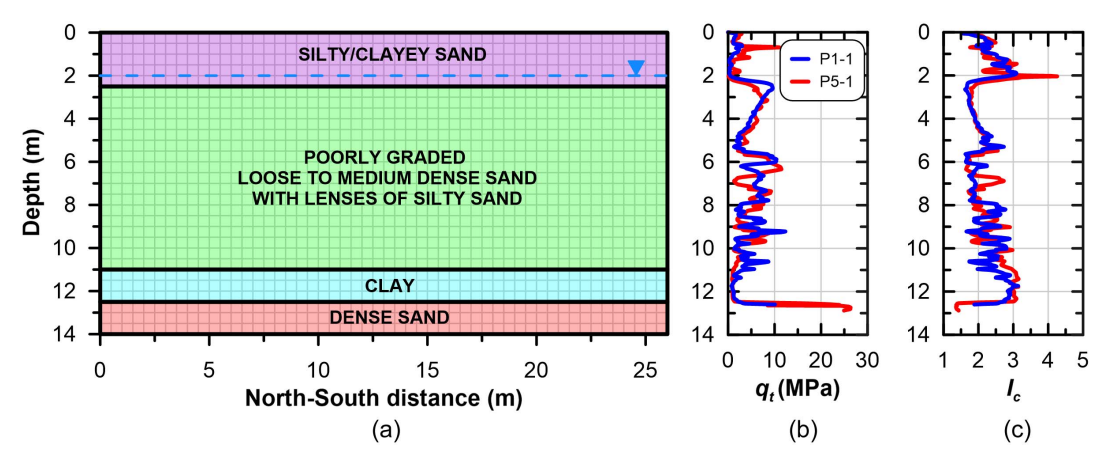


Fig. 2. (a) Cross section of the general soil section at Hollywood site along with the FLAC mesh; (b) q_I ; and (c) I_c measurements at two locations from CPT tests. (Adapted from Bong and Stuedlein 2017.)

densification and controlled blasting. Soundings within each grouping of five CPTs was initiated at the locations designated-1 (e.g., P1-1) and at the corner locations to reduce potential soil disturbance. Two typical cross sections (Sections 1 and 12) are marked in Fig. 1, and these are used for subsequent analysis in this paper.

The generalized stratigraphy at the Hollywood site is shown in Fig. 2(a). Two typical q_t and I_c profiles [Figs. 2(b and c), respectively] were determined using the seismic CPT tests P1-1 and P5-1 in Fig. 1. The upper 2.5 m is a loose to medium-dense silty or clayey sand fill, which overlies an 8.5-m-thick potentially liquefiable layer composed of loose to medium-dense poorly graded sand with lenses of silty sand which forms the focus of this study. The q_t and I_c values for this layer are consistent with those expected for clean sands or silty sands (Robertson and Wride 1998). The liquefiable layer is underlain by a 1.5-m-thick, soft to medium-stiff clay layer which in turn is underlain by a 1.5-m-thick dense sand layer. The thicknesses of the various layers generally are uniform across the site (Bong and Stuedlein 2018), and stratigraphic variability was not considered in this study. The depth to groundwater exhibited seasonal variation, and can be as shallow as 2 m below the ground surface.

Bong and Stuedlein (2018) used random field theory (Vanmarcke 1977) to produce a three-dimensional (3D) geostatistical model of q_t , FC, and q_{c1Ncs} within the liquefiable layer to account for the spatial variability of both the sand and the silty sand lenses. The geostatistical model was discretized vertically using 5-cm intervals from 2.5 to 11 m depth and 25 cm in horizontal directions (from 0 to 3 m in the east-west (E-W) direction and from 0 to 26 m in the north-south (N-S) direction), resulting in 13 cross sections of q_{c1Ncs} separated by a distance of 25 cm in the E-W direction. In contrast, the 2D numerical simulations used in this study averaged the original geostatistical discretization to produce grids with a 50-cm spacing in the vertical direction and a 50-cm spacing in the N-S direction to reduce the number of elements in the simulations and decrease computation time. The numerical simulations considered the same discretization interval of 25 cm in the E-W direction as the 3D geostatistical model, and all 13 cross sections were utilized for simulations. Two cross sections through the 3D model at 0 m (E-W direction) and 2.75 m (E-W direction), referred to as Sections 1 and 12, respectively, are shown in Figs. 3(a and b) as an example of the spatial variability in penetration resistance within the liquefiable layer at the site. Fig. 3(c) shows the cumulative distribution functions (CDFs) of q_{c1Ncs} for the 13s oil sections; differences were negligible. The median q_{c1Ncs} is 80 and standard deviation is 14.5.

Numerical Simulation Approach

Numerical simulations were conducted for the 13 soil sections running along the N-S direction (Fig. 2) with a width of 26 m and a total depth of 14 m. The simulations were performed using square elements of 50 cm in width (baseline conditions), which allow propagation of frequencies smaller than 28 Hz (Kuhlemeyer and Lysmer 1973). Additional soil columns on either side of the specified stochastic ROI were considered to better replicate the in situ free-field liquefaction response. The width of the extra soil columns was 78 m [three times the width of the ROI (26 m)] to reduce the effects of the boundaries (discussed in a subsequent section). Additional simulations were performed for five representative uniform soil sections with q_{c1Ncs} values equal to the median ($q_{c1Ncs} = 80$), 16th $(q_{c1Ncs} = 65.5)$, 33rd $(q_{c1Ncs} = 72.7)$, 67th $(q_{c1Ncs} = 87.3)$, and 84th percentiles ($q_{c1Ncs} = 94.5$) as obtained from the source CDFs (Fig. 3). The simulations used the numerical platform FLAC v8.0 and the nonlinear constitutive model PM4Sand v3.1 (Boulanger and Ziotopoulou 2017) for the sand layers, and the Mohr-Coulomb model for the clay layer.

Each simulation was performed in three stages. In the first stage, the model geometry, soil properties and boundary conditions were defined, and the geostatic stress state (static equilibrium) was achieved. The base of the model was fixed against movement, and only vertical movements along the sides of the model were allowed. Hydrostatic pore-pressure conditions were established across the model to match the depth of the ground water table (2 m below the ground surface). In the second stage of the analysis, earthquake shaking was applied to the base of the model as a horizontal acceleration time history. During this dynamic stage, the base of the model was fixed against vertical movement, and free-field boundary conditions were applied to the sides of the model. Drainage could take place from the model top, but the sides of the model were considered to be no-flow boundaries. Rayleigh damping of 0.5% centered at a frequency of 1 Hz was used to dampen numerical noise based on recommendations by Boulanger and Ziotopoulou (2017). In the final stage, boundary conditions at the model base and sides were the same as those used in the first simulation stage, and the model was allowed to reconsolidate until all the excess pore pressures generated during shaking had dissipated. Analyses for Section 12 were repeated using 25-cm element widths (half of the baseline) and half of the default time step in FLAC, and resulted in mean and maximum differential settlements that were almost identical to those of the simulation using the baseline conditions.

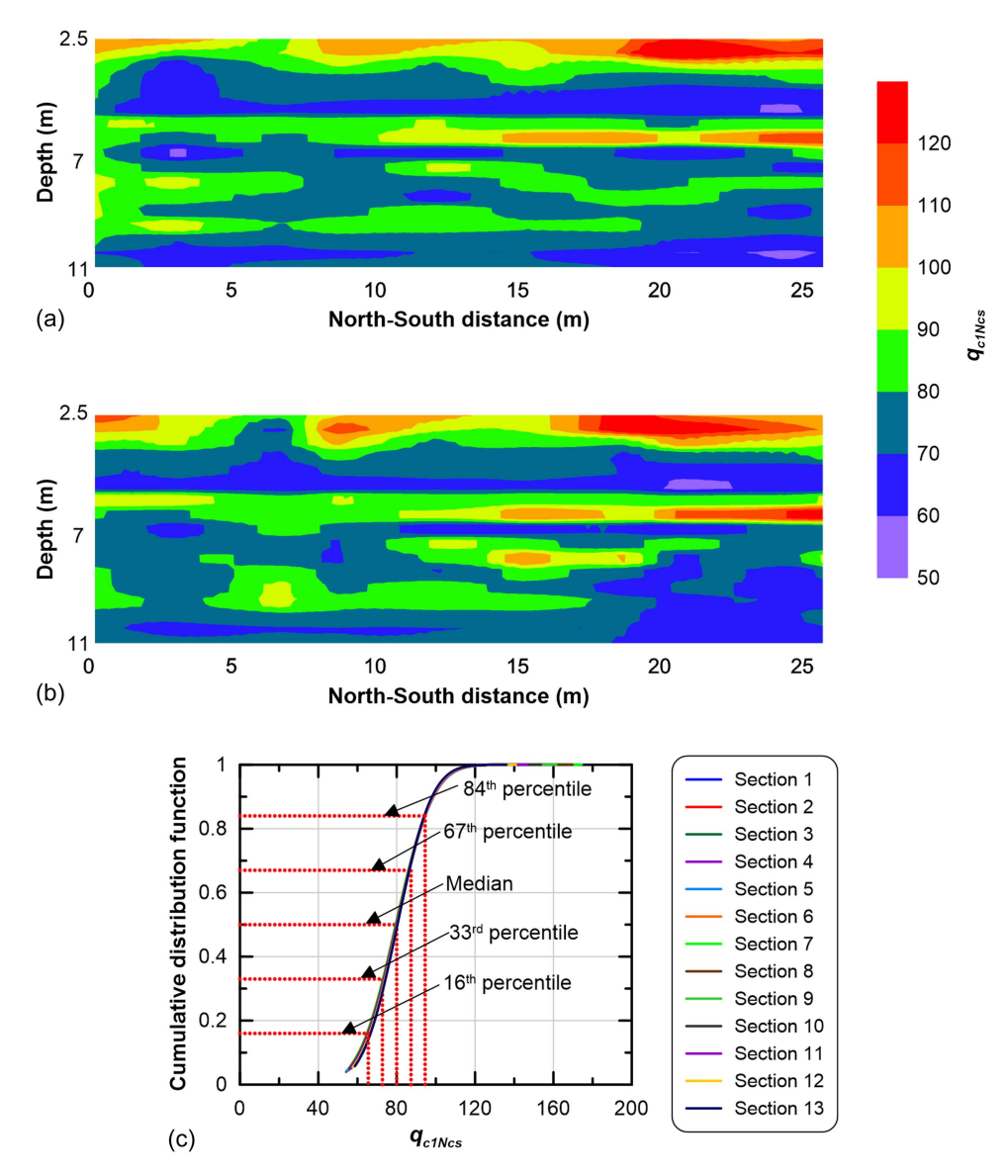


Fig. 3. (a) q_{c1Ncs} distribution at Section 1 in the E-W direction; (b) q_{c1Ncs} distribution at Section 12 in the E-W direction; and (c) cumulative distribution function of q_{c1Ncs} for each of the 13 sections at Hollywood.

Constitutive Models

The fill layer, liquefiable layer, and the dense sand layer at the model base were modeled using the stress ratio-controlled bounding surface plasticity model PM4Sand (v3.1, Boulanger and Ziotopoulou 2017), whereas the clay layer was modeled using the linear elastic perfectly plastic Mohr-Coulomb model. The dynamic response was modeled in PM4Sand using three primary parameters: D_r , the shear modulus coefficient (G_o) based on the maximum shear modulus (G_{max}) or shear wave velocity (V_s) , and the contraction rate parameter (h_{po}) . Parameters D_r and G_o were selected based on laboratory or field measurements, whereas h_{po} must be calibrated using single-element cyclic direct simple shear (DSS) simulations to obtain the desired cyclic strength. Continuum stress ratio-based models cannot capture postliquefaction reconsolidation strains that occur due to sedimentation (Ziotopoulou and Boulanger 2013; Howell et al. 2015) or excess pore-water pressure dissipation along a constant stress ratio path (Malvick et al. 2006), because this mechanism violates the plasticity condition that forms the basis of the model formulation (Dafalias and Manzari 2004). Ziotopoulou and Boulanger (2013) proposed an approach to compensate for this limitation by reducing the elastic modulus during the reconsolidation process to increase the value of ε_v , which is controlled through a flag (PostShake) activated during the reconsolidation phase of the simulations. PM4Sand was chosen as the constitutive model for the liquefiable layer in this study because it is one of the few models that have been shown to produce reasonable agreement with postliquefaction responses from centrifuge experiments (Basu et al. 2022a, b) and field sites (Ziotopoulou and Boulanger 2013). Capturing postliquefaction reconsolidation is a very challenging problem for most constitutive models used for liquefaction analyses (Ramirez et al. 2018), and the development and validation of additional models that can capture this behavior is an important area for future research.

Dynamic Properties

Stochastic properties were used for the liquefiable layer to isolate the effects of spatial variability in the liquefiable layer on settlement patterns, whereas all other layers in the model were assumed to have uniform properties. For the liquefiable layer, the primary model parameters were correlated with the q_{c1Ncs} in each zone using established correlations. Parameter D_r was estimated based on q_{c1Ncs} using the Idriss and Boulanger (2008) correlation

$$D_r = 0.465 \left(\frac{q_{c1Ncs}}{0.9}\right)^{0.264} - 1.063 \tag{1}$$

The stress normalized shear wave velocity (V_{s1})

$$V_{s1} = 37.895(q_{c1Ncs})^{0.3244} (2)$$

and G_o

$$G_o = 33.192(q_{c1Ncs})^{0.6487} (3)$$

also were correlated with q_{c1Ncs} by adjusting the default PM4Sand correlation between G_o and D_r to better match the average V_{s1} measured at the Hollywood site by Stuedlein et al. (2016) and Mahvelati et al. (2020). In contrast, h_{po} was calibrated to match the CPT-based cyclic resistance ratio [proposed by Boulanger and Idriss (2016)] to reach 3% single amplitude γ in 15 cycles (CRR_{15cyc}) in a cyclic DSS test (Fig. S1 in the Supplemental

Materials). This calibration process was repeated for 45 magnitudes of q_{c1Ncs} ranging from 30 to 250, which covered the range of q_{c1Ncs} value that exist in the geostatistical model. Values of h_{po} for intermediate q_{c1Ncs} values were obtained through linear interpolation. A reasonable upper limit of 0.8 was enforced on the calibrated CRR_{15cyc} for the very dense soils because the relationship by Boulanger and Idriss (2016) becomes asymptotic for q_{c1Ncs} values above approximately 180 and because the case history database for this relationship is limited to observed cyclic stress ratios below 0.6. The maximum void ratio (e_{max}), minimum void ratio (e_{min}), and hydraulic conductivity (k) were selected based on the recommendations by Gianella (2015), whereas the critical state friction angle (ϕ'_{crit}) was determined from DSS tests on Hollywood beach sand reported by Rauthause et al. (2020). The properties for the nonliquefiable layers are outlined in Table 1.

Reconsolidation Properties

The magnitude of the postshaking ε_v in PM4Sand is controlled by two reconsolidation calibration parameters, $f_{\rm sed,min}$ and $p_{\rm sed,o}$, which control the magnitude of modulus reduction and the range

Table 1. Uniform soil properties for nonliquefiable layers

·	Input properties								
Layer	$\overline{D_r}$	Cohesion (kPa)	$\phi'_{\rm crit}$ (degrees)	$\rho_d (\mathrm{kg/m^3})$	V_{s1} (m/s)	$e_{\rm max}$	e_{min}	G_s	k (cm/s)
Fill	0.7	_	33	1,481	188	1.1	0.65	2.65	0.01
Clay	_	38	0	1,500	168	_	_	_	0.0001
Dense sand	0.9	_	33	1,550	215	1.1	0.65	2.65	0.01

Note: ρ_d = dry density of soil; and G_s = specific gravity of solids.

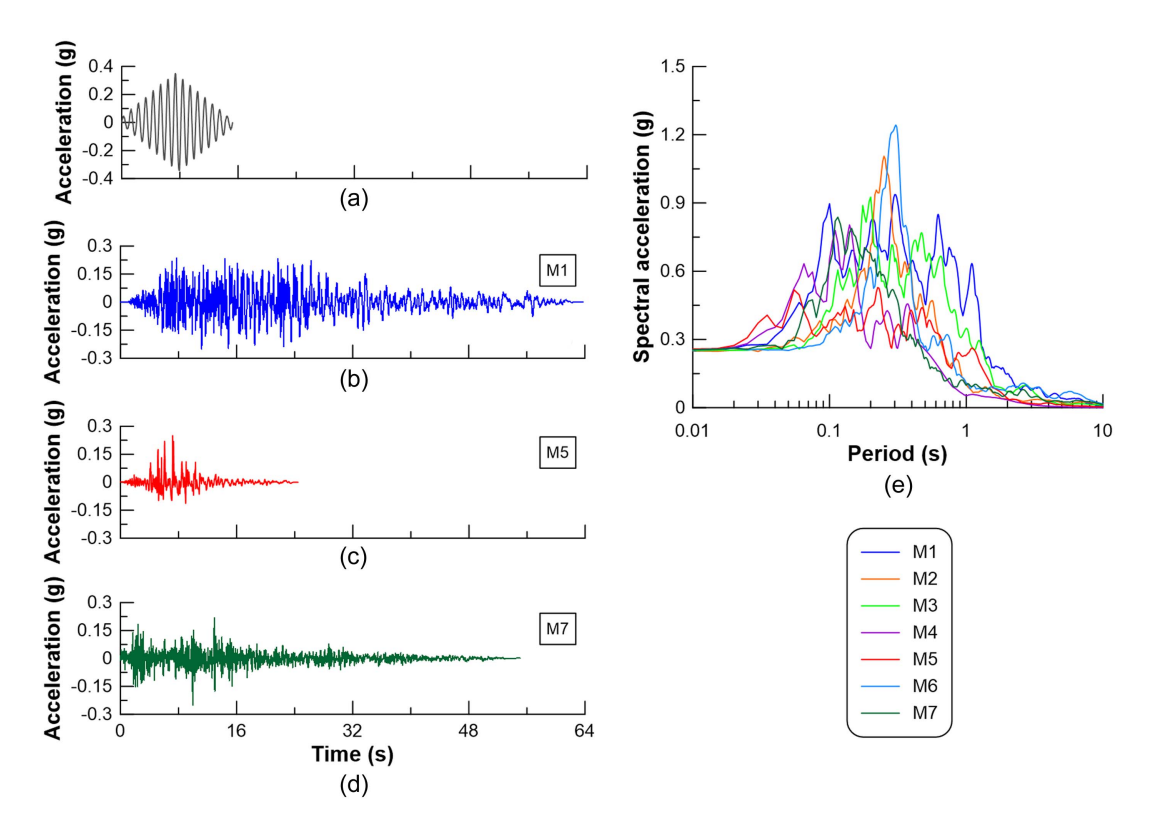


Fig. 4. Four typical input motions used in this study: (a) RS input motion with a PGA of 0.35*g*; and three linearly scaled recorded earthquake shaking: (b) M1, Imperial Valley-06; (c) M5, Victoria, Mexico; (d) M7, Sitka, Alaska; and (e) response spectra for the recorded earthquake motions used in this study scaled to a PGA of 0.25*g*.

Table 2. Characteristics of earthquake loadings considered in this study

	Recording			Total	Predominant	CAV (m/s)		I_a (m/s)	
Earthquake loading	station	Year	M_w	duration (s)	period (s)	$\overline{PGA} = 0.25g$	PGA = 0.53g	$\overline{PGA} = 0.25g$	PGA = 0.53g
M1: Imperial Valley-06	Cerro Prieto	1979	6.53	63.7	0.30	25.52	53.91	3.48	15.53
M2: Duzce, Turkey	Lamont 531	1999	7.14	41.5	0.26	9.41	19.89	1.05	4.71
M3: Taiwan SMART1(45)	SMART1 E02	1986	7.30	32.9	0.20	10.19	21.54	1.28	6.74
M4: Helena, Montana-01	Carroll College	1935	6.00	40.0	0.14	2.08	4.41	0.19	0.86
M5: Victoria, Mexico	Cerro Prieto	1980	6.33	24.4	0.06	3.87	8.18	0.31	1.39
M6: Duzce, Turkey	Mudurnu	1999	7.14	28.83	0.30	8.49	17.94	0.92	4.08
M7: Sitka, Alaska	Sitka Observatory	1972	7.68	55.0	0.12	10.57	22.33	0.86	3.83
Ramped sinusoidal ^a	_	_	_	15.0	1.00	12.84	_	2.57	

Note: CAV = cumulative absolute velocity; I_a = Arias intensity.

of mean effective stresses over which the reduction is active, respectively. Boulanger and Ziotopoulou (2017) selected a value of 20 kPa for $p_{\mathrm{sed},o}$, noting that ε_v was relatively insensitive to increases in $p_{\mathrm{sed},o}$ above 20 kPa. The D_r -dependent relationship for $f_{\mathrm{sed},\min}$, as described in PM4Sand v3.1 developed by Boulanger and Ziotopoulou (2017)

$$f_{\text{sed,min}} = A \cdot \exp(B \cdot D_r) \tag{4}$$

was implemented through calibration with the empirical relationship suggested by Ishihara and Yoshimine (1992), where A and B are constants, set to 0.03 and 2.6, respectively (Boulanger and Ziotopoulou 2017). Later versions of PM4Sand (v3.2 and v3.3) have suggested that a constant $f_{\rm sed,min}=0.04$ would produce reasonable responses in most cases, but they also have noted that users can select both $f_{\rm sed,min}$ and $p_{\rm sed,o}$ based on relevant soil-specific data.

Basu et al. (2022a) demonstrated that the use of a soil-specific calibration can improve estimates of reconsolidation settlements from centrifuge tests, and Basu et al. (2023) proposed a correlation between the A parameter and D_{50} for clean sands. Considering the lack of available postcyclic reconsolidation test data for Hollywood beach sand, a sensitivity analysis was conducted to estimate values of A that would produce a reasonable agreement with the freefield reconsolidation settlements measured at the site following controlled blasting experiments (Gianella and Stuedlein 2017). Although there is some uncertainty regarding the similarity and differences between the postliquefaction response of soil deposits subjected to multidirectional blast- and earthquake-induced ground motions, the use of the available full-scale, site-specific experimental reconsolidation settlement data was considered to be appropriate herein because the dynamic far-field response of sands to blasting motions is controlled by shear waves with frequencies which are within the range of earthquake ground motions (Jana and Stuedlein 2021; Stuedlein et al. 2023). The settlement obtained using the sitespecific A, along with the settlements simulated using the default and correlated A values from Basu et al. (2023) are discussed subsequently.

Effect of Liquefaction on Hydraulic Conductivity

Previous studies (Arulanandan and Sybico 1992; Jafarzadeh and Yanagisawa 1995; Shahir et al. 2012) suggested that liquefaction results in an increase in hydraulic conductivity due to loss of contact between soil grains in its liquefied state. As the liquefied soil reconsolidates, the contacts between grains are re-established and the hydraulic conductivity returns to some magnitude that may or may not reflect its initial fabric. In this study, a sensitivity analysis was conducted using the excess pore-pressure ratio (r_u) -dependent

variable k model developed by Shahir et al. (2012) to investigate the effect of variation in k on reconsolidation responses; r_u is defined as the ratio of excess pore pressure to initial vertical effective stress. The hydraulic conductivity relationship for the dynamic phase is

$$\frac{k_m}{k_i} = 1$$
 $r_u \le 0 = 1 + (\alpha - 1) \times r_u^{\beta_1}$ $r_u \le 1 = \alpha$ $r_u > 1$ (5)

whereas the relationship for the reconsolidation phase is given by

$$\frac{k_m}{k_i} = 1 \quad r_u \le 0 = 1 + (\alpha - 1) \times r_u^{\beta_2} \quad r_u \le 1 = \alpha \quad r_u > 1$$
 (6)

where k_i = initial hydraulic conductivity at $r_u = 0$; k_m = modified hydraulic conductivity; α is the factor by which hydraulic conductivity increases at $r_u = 1.0$; and β_1 and β_2 control the rates at which hydraulic conductivity increases and decreases with r_u during and following shaking, respectively. The hydraulic conductivity remains constant for r_u conditions above 1.0, which may occur due to changes in total stress as the soil mass deforms, although this did not occur in the simulations in this study. Exponents β_1 and β_2 were set to 1 and 2, respectively, whereas $\alpha = 17$ was used for Hollywood sand based on the correlation with D_{10} developed by Basu et al. (2022a). A simulation was performed for one of the cross sections using a constant hydraulic conductivity, wherein the postshaking dissipation rate decreased considerably compared with the corresponding variable hydraulic conductivity simulation, but the mean and maximum differential settlements differed by less than 3% between the two cases. This result agrees with the findings of Basu et al. (2022a), who found that variable conductivity had a

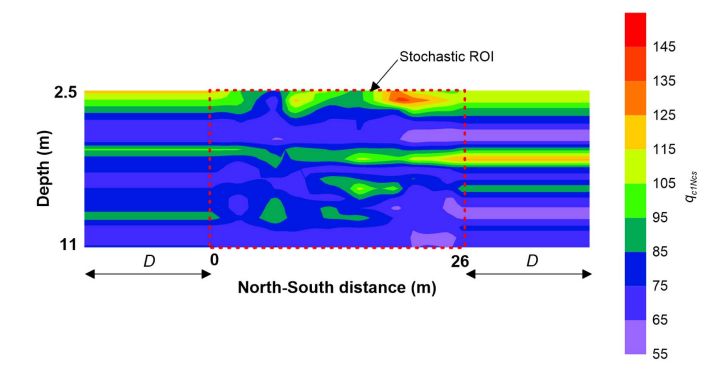


Fig. 5. Typical cross section used in numerical simulations showing the additional soil columns on either side of the stochastic ROI. The q_{c1Ncs} values shown here correspond to those from Section 12.

^aSynthetic, pseudo-harmonic loading with PGA = 0.53g was not considered for ramped sinusoidal loadings.

significant impact on dissipation rate, but a minimal impact on the magnitude of the settlement.

Input Motions

Synthetic pseudo-harmonic ramped sinusoidal (RS) loading and recorded earthquake shaking [Figs. 4(a–d)] were used as input motions for the simulations in this study to parametrically investigate

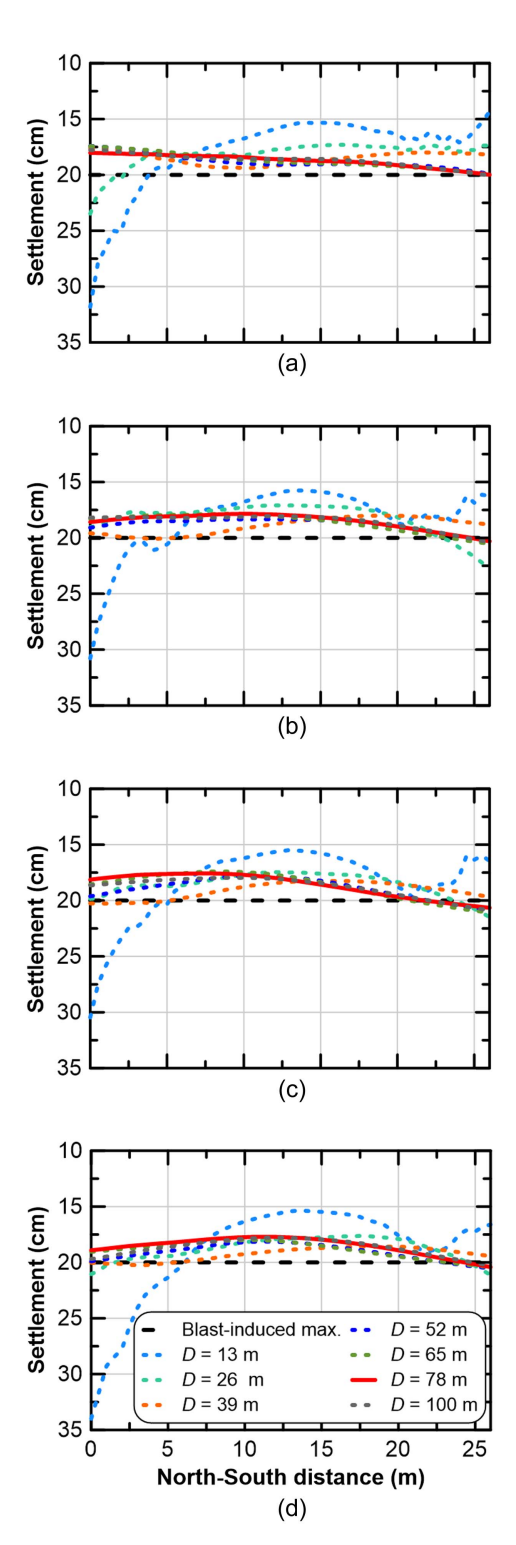


Fig. 6. Settlement profiles for various D obtained from simulations of sections in the E-W direction using free-field boundary conditions: (a) Section 1; (b) Section 5; (c) Section 8; and (d) Section 12.

the effects of motion intensity (as in the case of RS motions), frequency, and duration (as in the case of recorded earthquake motions) on reconsolidation settlements of the stochastic sections. The RS motions had a duration and frequency of 15 s and 1 Hz, respectively, and seven magnitudes of peak ground acceleration (PGA)—0.05, 0.13, 0.25, 0.35, 0.45, 0.6, and 0.7 g—were considered in order to assess the role of intensity on mean and maximum differential settlement. The fault-normal components of seven recorded earthquakes were chosen from the suite of motions (referred to as Set 1A: broad-band ground motions) recommended by Baker et al. (2011) to approximate a strike-slip event with a moment magnitude (M_w) of 7 at distance of 10 km. This event approximately represents the M_w and closest distance to rupture plane (R_{rup}) combination for the most probable earthquake events expected at the Hollywood site that correspond to return periods of 475 and 975 years as determined using the Unified Hazard Tool (USGS 2014). Moreover, the most severe earthquake in the vicinity of the Hollywood area, the 1886 Charleston earthquake (Nuttli et al. 1986), also corresponded to $M_w = 7$ with an epicentral distance of 30 km from the Hollywood site. These seven selected motions were recorded at rock sites and have a range of spectral shapes [Fig. 4(e)]. Each of these motions was scaled linearly to produce

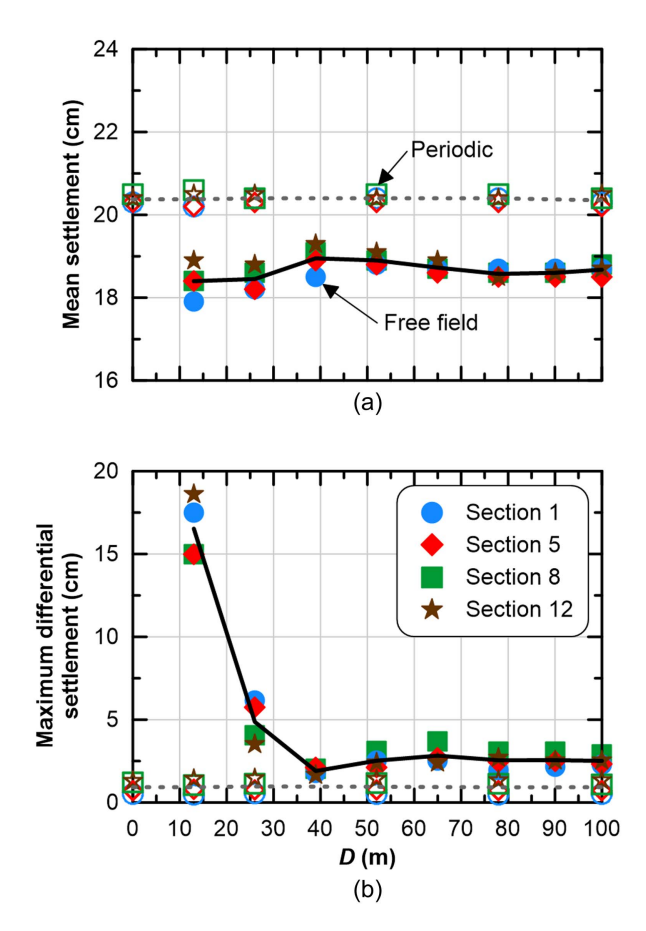


Fig. 7. Variation of settlements with *D* for four sections each using two different lateral boundary conditions: (a) mean settlement; and (b) maximum differential settlement. Hollow symbols and dotted lines correspond to simulations using periodic boundary condition; solid symbols and solid lines correspond to simulations using free-field boundary condition. Periodic boundaries tend to overpredict mean settlement and underpredict differential settlement relative to the more-realistic free-field boundaries.

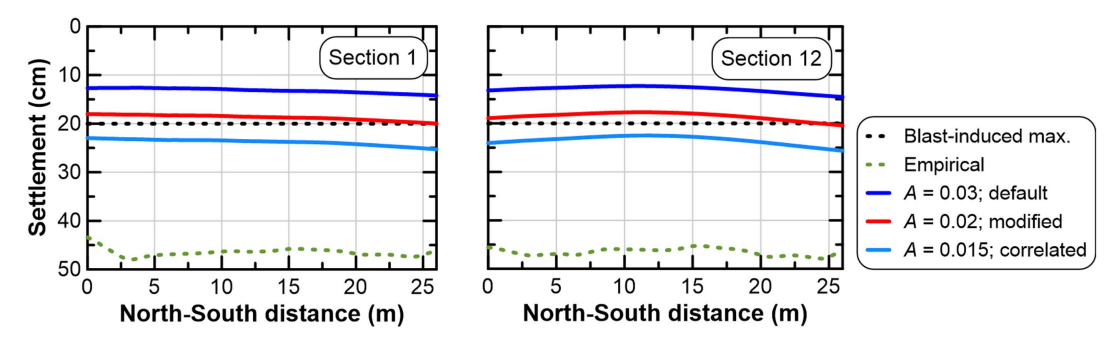


Fig. 8. Settlement profiles from simulations of two cross sections in the E-W direction using default and modified relationships for $f_{\text{sed,min}}$ plotted alongside the blast-induced maximum settlement. Simulations used the baseline free-field boundary conditions with D=78 m.

PGAs of 0.25 and 0.53g that correspond to probability of exceedances of 10% (475-year return period) and 5% (975-year return period) in 50 years. Table 2 lists some of the important characteristics of the selected recorded earthquake records.

Sensitivity Analysis

Early simulation attempts indicated that the boundary conditions and $f_{\rm sed,min}$ parameter produced a significant impact on the

computed settlements. A sensitivity analysis was carried out to investigate these effects, and the settlement results were compared with the maximum settlement observed from a blast-induced liquefaction study performed at the site (Gianella and Stuedlein 2017). All the simulations described in this section were subjected to a RS input motion (1 Hz and 15 cycles) with a PGA of 0.7g. The I_a value of this input motion was 21 m/s, which is similar to the I_a value estimated for the blast event (Gianella and Stuedlein 2017).

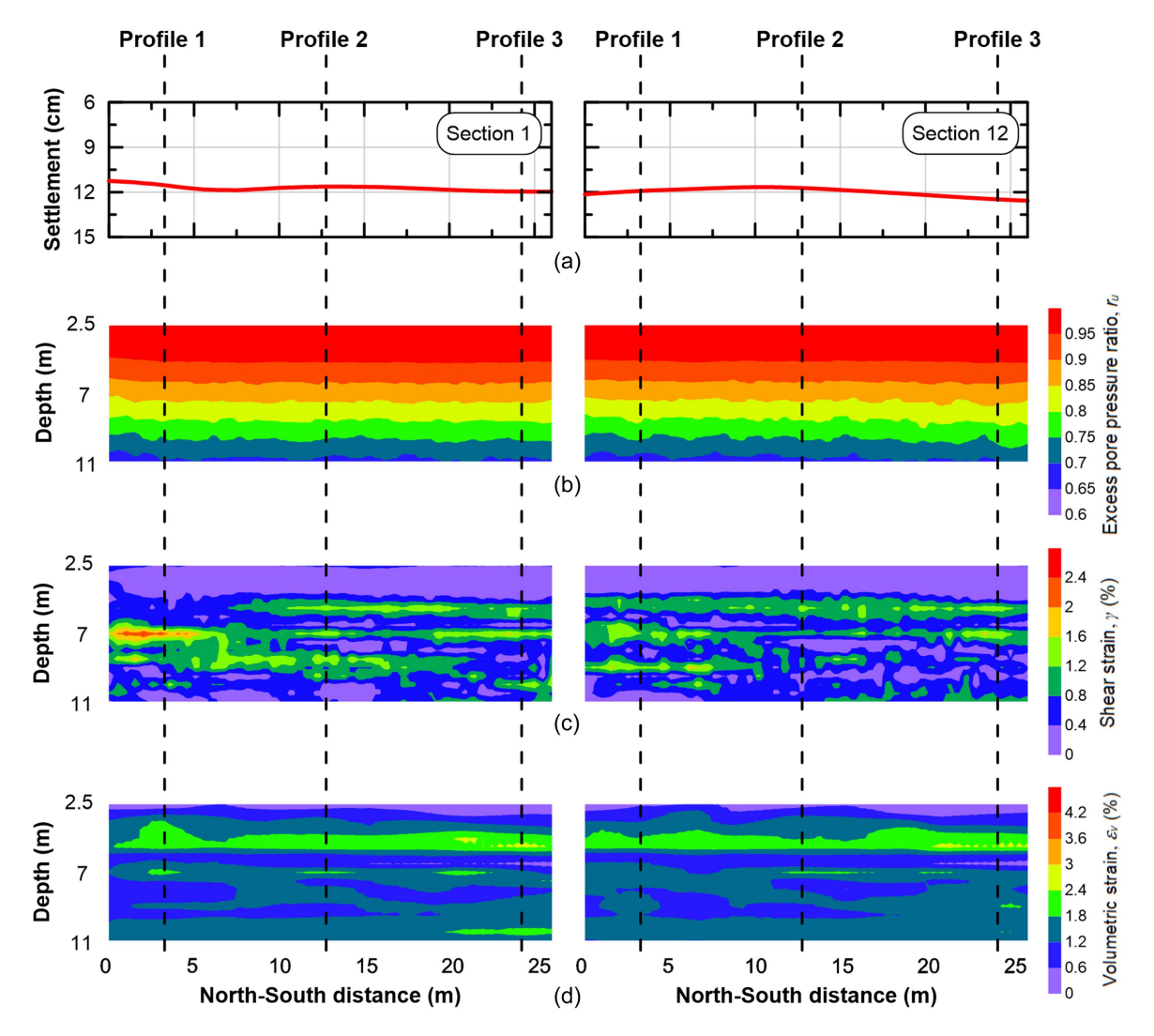


Fig. 9. Responses from two simulations of soil Sections 1 and 12 in the E-W direction: (a) settlement; (b) end-of-shaking r_u ; (c) end-of-shaking γ ; and (d) postreconsolidation ε_v . Both simulations were subjected to the RS input motion with a PGA of 0.13g.

Effect of Lateral Boundary Conditions on Settlement

Simulations were performed using both free-field (baseline) and periodic boundary conditions along the lateral sides of the model. The free-field boundary condition seeks to approximate a 1D response along the sides of the model, and is described by Itasca (2016). A linear elastic constitutive model was assigned to the elements forming two columns on either edge of the section, with properties identical to those from the adjacent columns that utilized the PM4Sand model. The periodic boundary condition enforced identical displacements at each side of the model, and commonly is used for infinite-slope conditions (e.g., Montgomery and Boulanger 2017). For both sets of simulations, additional soil columns were used on either side of the stochastic ROI up to the lateral boundaries to evaluate the effect of lateral γ smearing as a result of the boundary condition. Separation distances (D) of 13, 26, 39, 52, 65, 78, 90, and 100 m from the lateral boundaries were utilized for the simulations (Fig. 5). The soil properties from the columns on either edge of the stochastic ROI were used for the additional columns to imply lateral continuity in the free-field and isolate the stochastic variability within the ROI. Similar exercises of isolating the ROI from lateral boundaries in numerical models were conducted by Chian et al. (2014) and Pretell et al. (2022).

Fig. 6 shows the settlement profiles for various D values obtained from simulations of cross sections at distances of 0 (Section 1), 1 (Section 5), 1.75 (Section 8), and 2.75 m (Section 12) in the E-W direction using the baseline free-field boundary condition. When the boundaries were close to ROI ($D \leq ROI$ width), the boundary conditions led to much larger settlements along the north edge of the model and lower settlements along the south edge of model compared with those at larger separation distances for all four cross sections; thus, the distance separating the ROI from the vertical boundary impacts the magnitude of maximum differential settlement when using free-field boundary conditions. The mean and maximum differential settlements (calculated as the difference between the maximum and minimum settlements obtained from a stochastic section) for each of the simulations are shown in Fig. 7. For free-field boundaries, convergence of settlements was observed for D = 78 m (three times the width of the ROI) and greater (Fig. 7). Thus, a D value of 78 m (baseline) was selected for all subsequent simulations. This ratio of D with respect to the width of the ROI was slightly greater than the value of 2.50 (D = 250 m, ROI width = 100 m) that Pretell et al. (2022) found appropriate for their study. The larger D/ROI width ratio that was required for this study possibly could be a result of the nonlinearity

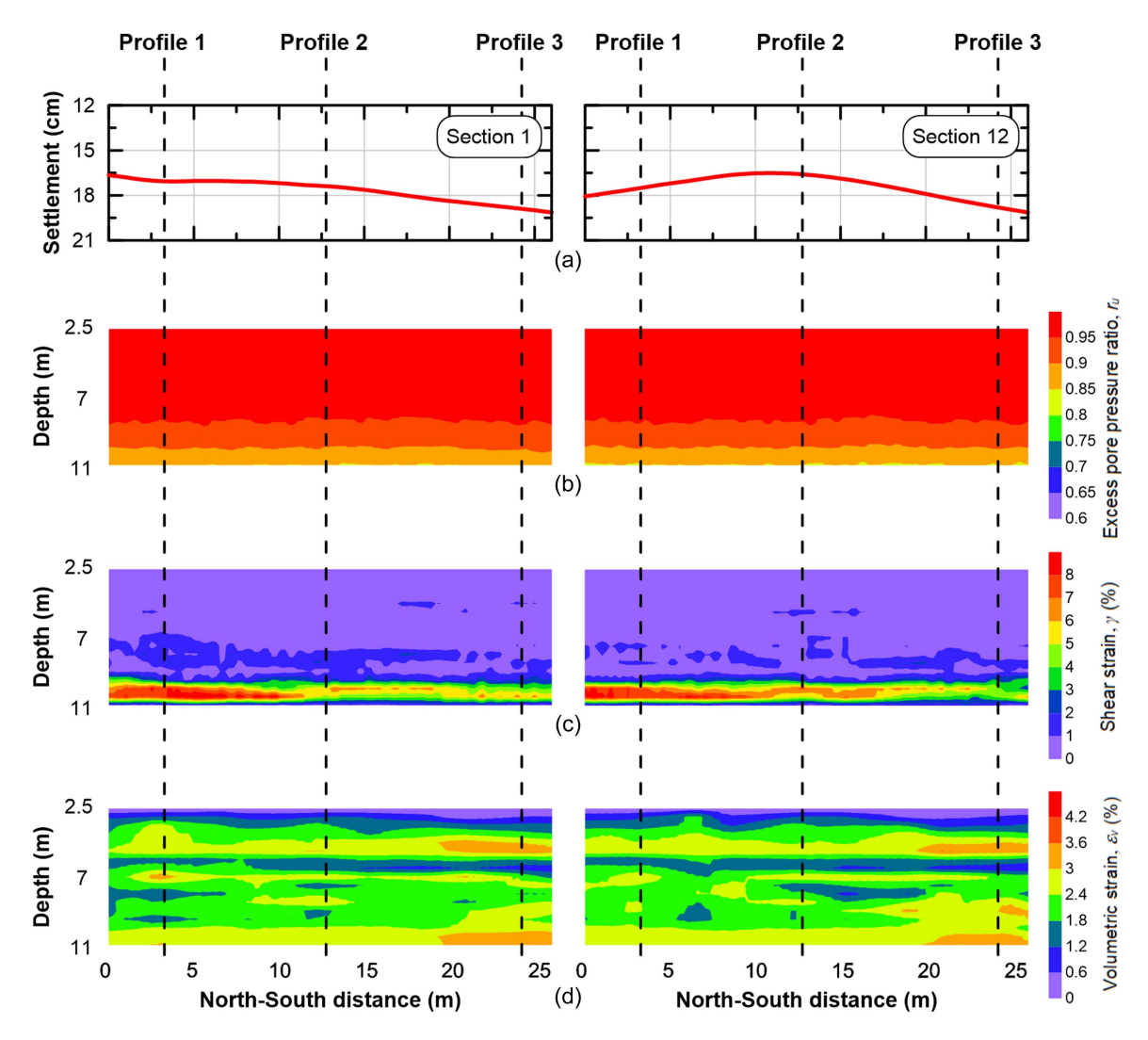


Fig. 10. Responses from two simulations of soil Sections 1 and 12 in the E-W direction: (a) settlement; (b) end-of-shaking r_u ; (c) end-of-shaking γ ; and (d) postreconsolidation ε_v . Both simulations were subjected to the RS input motion with a PGA of 0.35g.

in the numerical model used herein, unlike the linear elastic model used by Pretell et al. (2022).

The effect of using periodic boundary conditions on the lateral edges of the model on settlements also was evaluated. Periodic boundary conditions are meant to simulate infinite-slope boundaries (Montgomery and Boulanger 2017) and attached boundaries such as those imposed by laminar centrifuge containers (Basu et al. 2022a), but are not intended to capture free-field conditions. Despite this, periodic boundaries have been used in recent numerical analyses of liquefaction-induced deformations, so the effect of these boundaries on the response was examined. In this study, the mean and maximum differential settlements from simulations using periodic boundary conditions were insensitive to D (Fig. 7). The periodic boundaries overpredicted the mean settlement (by approximately 2 cm) and underpredicted the differential settlement (2-4 times lower) compared with the more realistic free-field boundary conditions [Fig. 7(b)]. This occurs because the periodic boundary conditions lead to larger and more-uniform γ values across the model due to the tied displacement degrees of freedom along the edges. Although this boundary condition is computationally efficient and insensitive to separation distance, it is meant to simulate infinite slope conditions and is not representative of level ground conditions, and therefore was not considered further in this study. These results highlight that the use of this boundary may provide misleading results when applied to spatially variable sites.

The characteristics of the model base boundary govern pertinent aspects of site response. Mejia and Dawson (2006) provided a comprehensive review of the dynamic boundary conditions available in FLAC and how to properly select a base location (e.g., depth and thickness) and deconvolution procedure to perform a site response analysis. The present study does not focus on reproducing a specific surface motion given an input motion, and so the type and location of the bottom boundary remained fixed throughout the simulations. An analysis was performed using a thicker dense sand layer (7.5 m versus the 1.5 m used in the baseline analyses), and no significant change was observed in the response of the liquefiable layer or the surface settlements.

Effect of $f_{\text{sed,min}}$ on Settlement

Early simulations indicated that the default reconsolidation parameters underpredicted the settlement relative to the results from the blast-induced liquefaction study (Fig. 8). The constant A in the relationship for $f_{\rm sed,min}$ [Eq. (4)] was modified iteratively to 0.02 to better fit the maximum blast-induced settlement observed (Fig. 8). The correlation developed between A and D_{50} by Basu et al. (2023) for clean sands produces A = 0.015 corresponding to the mean D_{50}

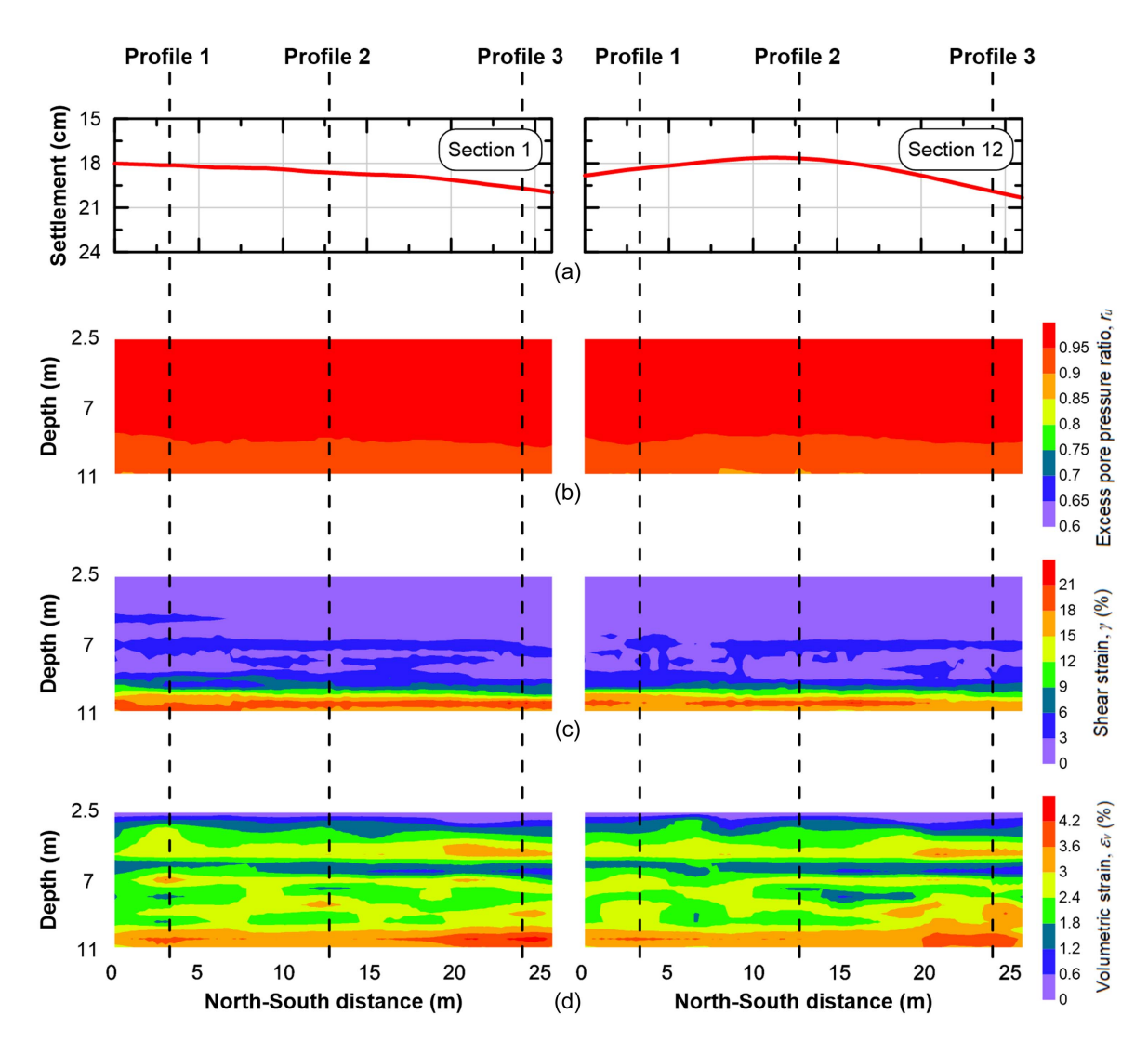


Fig. 11. Responses from two simulations of soil Sections 1 and 12 in the E-W direction: (a) settlement; (b) end-of-shaking r_u ; (c) end-of-shaking γ ; and (d) postreconsolidation ε_v . Both simulations were subjected to the RS input motion with a PGA of 0.7g.

of 0.18 mm for Hollywood sand (Gianella 2015). Basu et al.'s (2023) correlation was developed using different clean sands with D_{50} ranging from 0.19 to 0.34 mm, so the power-law correlation was extrapolated to calculate A for this site. Fig. 8 also shows empirical estimates of settlement computed using the Yoshimine et al. (2006) correlation (assuming $M_w = 7.5$ and PGA = 0.7g, as was used in the RS motions), which were significantly larger than either the observations or simulations. The simulations using the default A value from PM4Sand underpredicted the maximum observed settlement, whereas the simulations utilizing the A value from Basu et al. (2023) overpredicted the observed settlement. The calibrated value (A = 0.02) offers the best match to the field observations and was used for the remaining simulations described in this study. The recommended default value of 20 kPa for $p_{\text{sed},o}$ (Boulanger and Ziotopoulou 2017) was used in all the simulations performed in this study.

Results

Simulations were performed for all 13 sections using both RS and recorded earthquake input motions scaled to different PGAs. Detailed results are presented for the two stochastic Sections 1 and 12. These sections were selected because of the noticeable difference in the shape of the simulated settlement profiles between them (Fig. 6). The corresponding tip resistance contours are shown in Fig. 3.

Soil Responses from Two Stochastic Sections Subjected to Ramped Sinusoidal Motions

Fig. 9 presents the reconsolidation settlement, end-of-shaking r_u and γ , and postreconsolidation ε_v from simulations of stochastic soil Sections 1 and 12 for the RS input motion with PGAs of 0.13g. Results for 0.35 and 0.7g are shown in Figs. 10 and 11, respectively. All simulations used the baseline conditions (50-cm elements with free-field boundaries located 78 m from the ROI). The mean settlement was similar for both soil sections at a given PGA but exhibited differing differential settlement profiles as a result of the spatial variability of the liquefiable layer [Figs. 9(a), 10(a) and 11(a)]. The simulation of Section 12 resulted in a larger maximum differential settlement (2.7 cm versus 1.96 cm at a PGA of 0.7g) than those of Section 1. The mean and differential settlement patterns are discussed subsequently.

Initial liquefaction with $r_u = 0.95-1.00$ often is defined as the criterion that governs the onset of liquefaction (Seed and Lee 1966). High r_u values were observed at the end of shaking at shallow depths for all three PGAs [Figs. 9(b), 10(b) and 11(b)], and the thickness of this region increased with an increase of input motion PGA. The simulations performed using the motion with a PGA of 0.7g had r_u values above 0.85 across the entire stochastic soil section at the end of shaking [Fig. 11(b)]. These figures show the excess pore pressures at the end of shaking, but some dissipation and redistribution of excess pore pressures occur during shaking, leading to a reduction in r_u (Fig. S2 in the Supplemental Materials), especially near the base of the liquefiable layer. No significant variation in r_u was observed laterally for any of the PGAs, as indicated by the r_u values at the three vertical profiles chosen at distances of 3.25, 12.75, and 24.25 m along the N-S direction (Fig. S3 in the Supplemental Materials). This can be verified further through the overlapping of r_u histories observed at five adjacent FLAC zones within the model at which q_{c1Ncs} varied between 68 and 100 (Fig. 12).

The magnitude of ε_v during reconsolidation is correlated with the magnitude of γ during shaking (Ishihara and Yoshimine 1992;

Yoshimine et al. 2006). Simulations using the RS motion with PGA = 0.13q exhibited relatively low γ values (<2.5%) with concentration of strain in a few localized zones [Fig. 9(c)] in which q_{c1Ncs} values were relatively low (Fig. 3). This pattern of γ distribution is similar to that observed by Montgomery and Boulanger (2017) for gently sloping ground, in which γ values were observed to localize in a path of interconnected weaker zones when liquefaction was triggered. The simulations with PGA = 0.35 [Fig. 10(c)] and 0.7g [Fig. 11(c)] exhibited significant shear strain concentration at a depth of about 10 m for both the soil sections with maximum γ of ~10% and ~20%, respectively, corresponding to a band of soil in which q_{c1Ncs} values ranged between 50 and 70 (Fig. 3). At these higher shaking PGAs, conditions close to initial liquefaction conditions ($r_u > 0.95$) can be observed almost throughout the entire soil section except in the bottom 2-3 m, where the shear strain was concentrated. This γ concentration at the base likely was due to attenuation of the seismic energy by the liquefied region above, as evident from the acceleration time histories (Fig. 13). Vertical profiles of γ are shown in Fig. 14. At the lower PGA of 0.13g, only

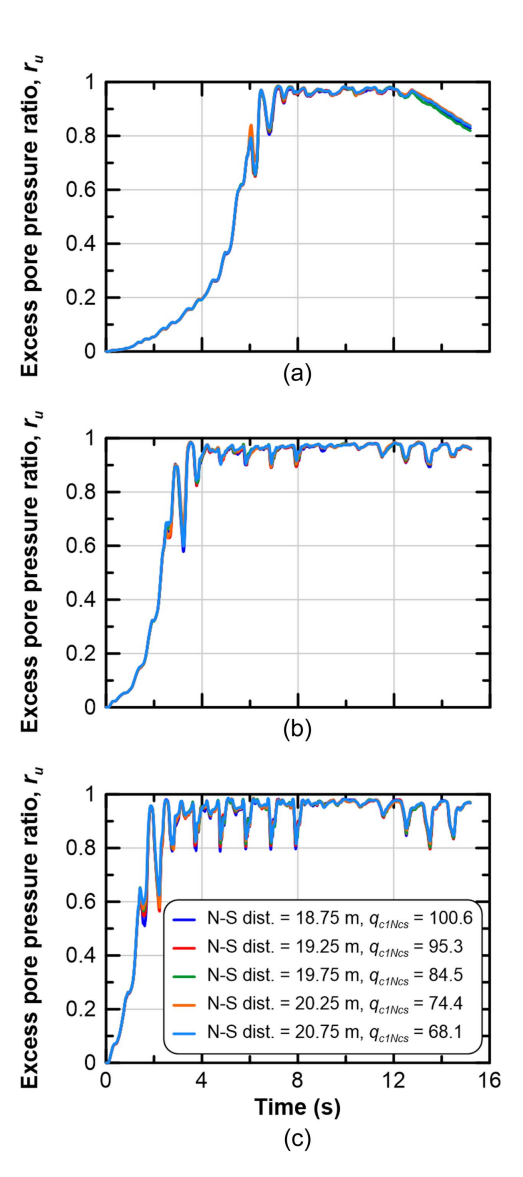


Fig. 12. Time histories of r_u at five adjacent FLAC zones along the N-S direction at a depth of 7.75 m using RS motions with PGAs of (a) 0.13g; (b) 0.35g; and (c) 0.7g. All simulations correspond to Section 12.

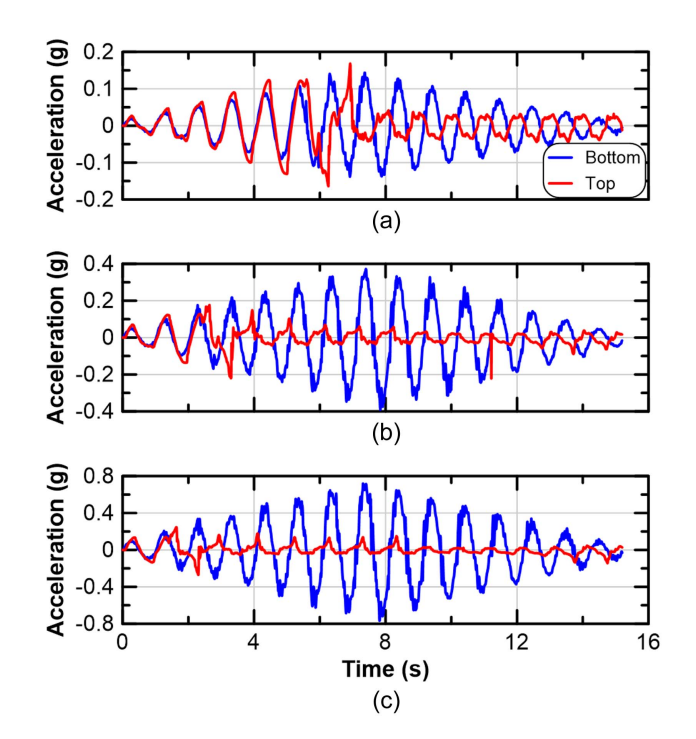


Fig. 13. Acceleration time histories at the bottom and top of the liquefiable layer from simulations using RS motions with PGAs of (a) 0.13g; (b) 0.35g; and (c) 0.7g. All simulations correspond to Section 12.

slight variation in γ occurred across the section, whereas at the higher shaking PGAs of 0.35 and 0.7g, γ varied by as much as 5% laterally at the shear bands (Fig. 14).

Figs. 9(d)–11(d) indicate that ε_v was concentrated in zones that corresponded to low q_{c1Ncs} values for the three PGAs and two sections considered. Nagase and Ishihara (1988) reported test results on Fuji River Sand with $D_r=47\%$ that exhibited an increase in ε_v to ~4% with an increase in maximum γ to ~10%, upon which ε_v became asymptotic. The same maximum ε_v , ~4%, also was observed in the simulations that used input motions with PGAs of 0.35 and 0.7g. The average ε_v across the soil sections increased by ~0.75% with an increase in input motion PGA from 0.13 to 0.35g. However, ε_v increased by a lesser extent, 0.2%, when PGA increased further from 0.35 to 0.7g.

The similar ε_v values noted for simulations with PGA = 0.35 and 0.7g led to similar mean settlements. This trend can be explained partially by examining the acceleration time histories recorded at the bottom and top of the liquefiable layer (Fig. 13). In both sections, the weakest zone was near the bottom of the profile. When this region liquefied, the reduction in stiffness led to damping of the seismic energy and a reduction in the loading on the shallower zones. For the PGA of 0.13g, this reduction occurred around the time of peak intensity (\sim 7 s), whereas it occurred after only 5 s of loading at 0.35g and 3 s of loading at 0.7g. The ratio of I_a of the recorded motions at the top and bottom of the liquefiable layer decreased from 0.69 to 0.09 as the PGA increased from 0.13 to 0.35g, and it decreased further to 0.03 as the input motion PGA increased to 0.7g. This demonstrates that the settlement

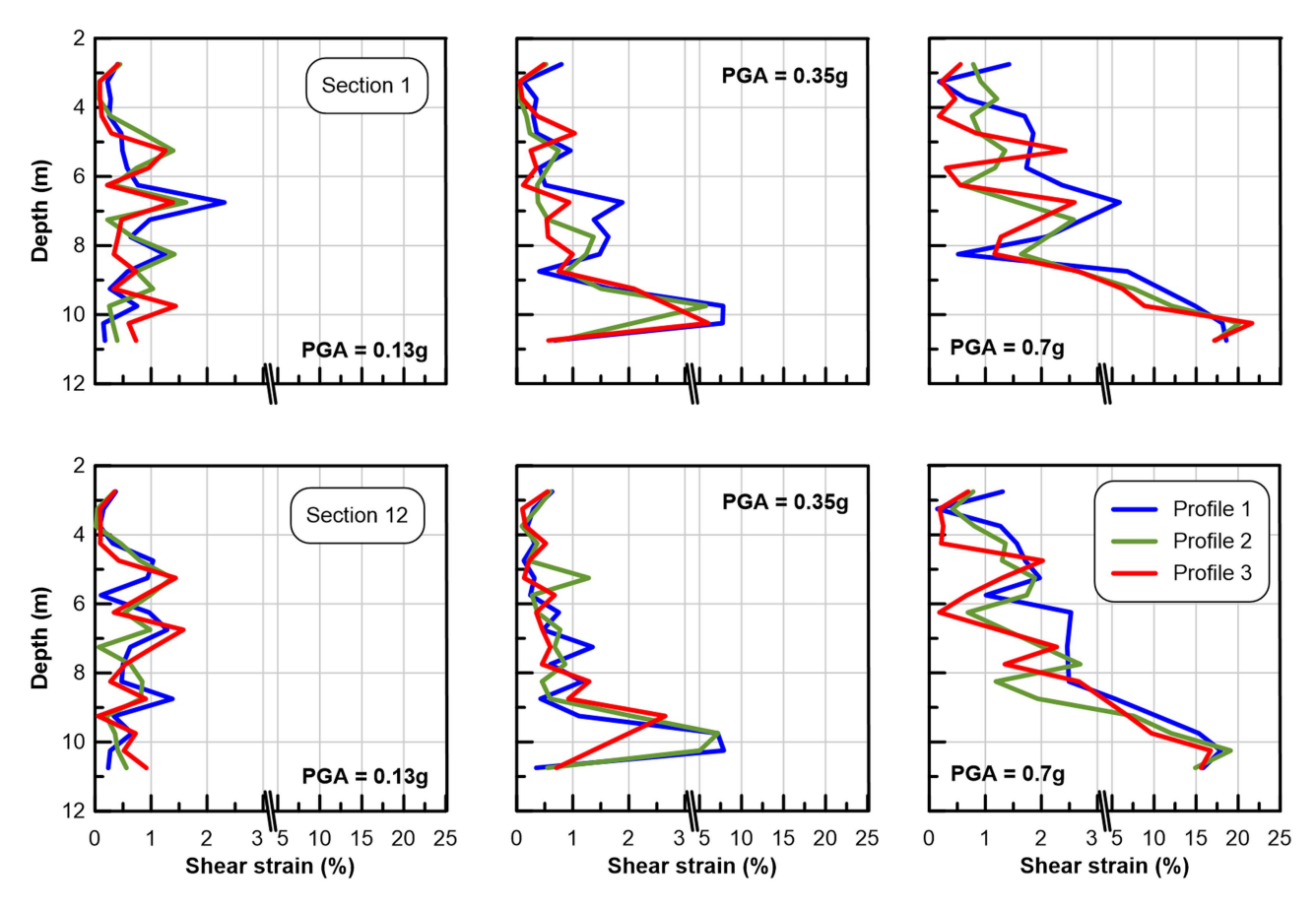


Fig. 14. End-of-shaking γ variation with depth at three vertical profiles along the N-S direction obtained from the simulations. Note the change in scale at $\gamma = 4\%$.

patterns are dependent not only on the distribution of q_{c1Ncs} within a soil section, but also on the intensity of the motion, and, subsequently, on the values of r_u and γ generated within the soil section.

Mean and Maximum Differential Settlements: Ramped Sinusoidal Motions

The previous discussion noted that mean settlements were similar for the two stochastic sections, but the settlement patterns varied, and depended on PGA. The mean and maximum differential settlements for all 13 stochastic sections are shown in Figs. 15(a and b), respectively. The mean settlements from these stochastic models are compared with those obtained from uniform models assuming representative q_{c1Ncs} which exhibited negligible differential settlements. Mean settlements were observed to increase at a decreasing rate with increases in PGA to 0.6g [Fig. 15(a)], after which the mean settlements did not change appreciably with increasing PGA. At any particular PGA, the mean settlements from the various stochastic sections did not vary significantly from each other. At all PGAs, a uniform model using the median q_{c1Ncs} reasonably would predict the mean settlement from the stochastic models, consistent with the findings of Montgomery and Boulanger (2017).

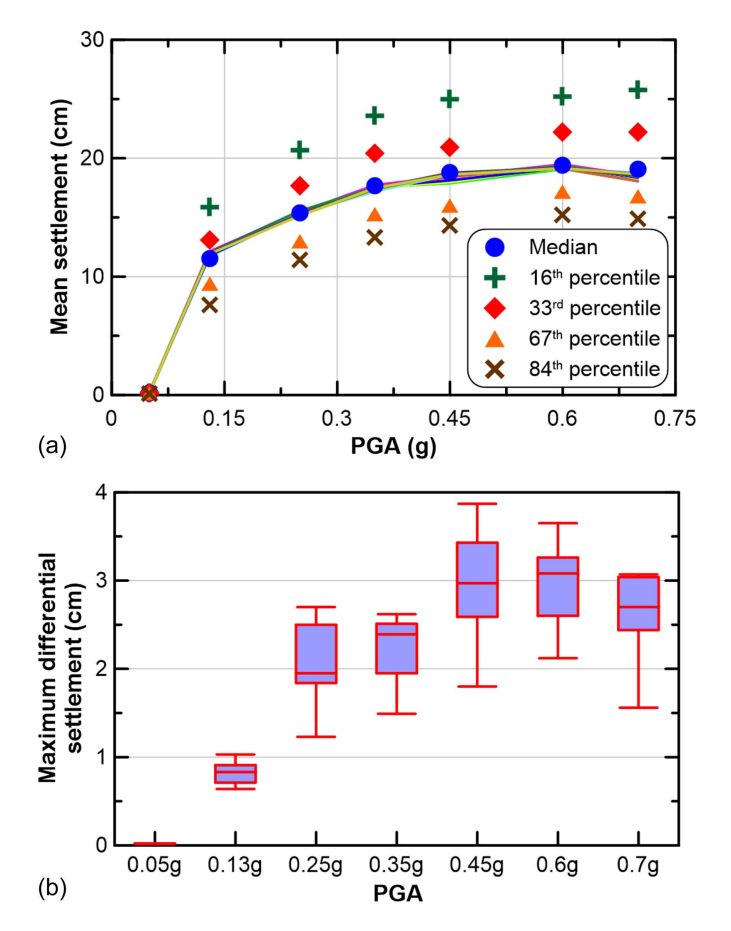


Fig. 15. (a) Variation of simulated mean reconsolidation settlements from the stochastic sections and the settlements from uniform sections with PGAs of the RS input motion, where solid lines represent the mean settlements from the stochastic sections, and symbols correspond to the settlements from the uniform sections using different percentile q_{c1Ncs} values; and (b) maximum differential settlements from simulations of all 13 stochastic sections using RS motions with different PGA levels.

The maximum differential settlement also tended to increase with input motion PGA and therefore mean settlement [Fig. 15(b)]. The largest spread in maximum differential settlement estimates among the 13 sections occurred in the simulation with PGA = 0.45g and decreased slightly at higher PGAs, which is attributed to more-uniform strain distributions at higher PGAs as both loose and dense zones liquefy. The maximum differential settlement as a percentage of the mean settlement varied from 5.3% to 8.6% at a PGA of 0.13g, from 10% to 20.8% at a PGA of 0.45g, and from 8.4% to 17% at a PGA of 0.7g.

Empirical estimates of maximum differential settlement using the Yoshimine et al. (2006) framework for the Hollywood site reported by Bong and Stuedlein (2018) indicated an opposite trend from that shown in Fig. 15(b), with higher maximum differential magnitude estimated at low PGAs (e.g., 12.8 cm at 0.11g) and a decrease in magnitude of maximum differential settlement with an increase in PGA (e.g., 10.2 cm at 0.15g, and 8.3 cm at 0.3g): simplified triggering analyses represent 1D assessments, and cannot capture system responses (Cubrinovski et al. 2019). Furthermore, the magnitudes of empirical estimates of maximum differential settlement also were 2-10 times larger than those obtained numerically from the stochastic simulations over the range of PGAs. The simulations described herein allowed for excess pore-pressure redistribution, which served to reduce the magnitude of maximum differential settlement anticipated from simplified 1D empirical estimates.

Effect of Recorded Earthquake Motions

Simulations also were conducted using the selected suite of recorded earthquake motions to assess how differences in duration and frequency content might influence the spatial distribution of settlement further. Figs. 16 and 17 present the spatial distribution of settlement, end-of-shaking r_u and γ , and postreconsolidation ε_v for the stochastic soil Section 12 using Motions M1 and M5 with PGAs of 0.25 and 0.53g. Despite their shared PGA, the mean settlement obtained from the simulations using Motion M1 was much larger than that obtained using Motion M5 [Figs. 16(a) and 17(a)], owing to its increased duration, cumulative absolute velocity (CAV), and I_a (Fig. 4 and Table 2). Widely used empirical liquefaction triggering and reconsolidation settlement models are unable to capture the complexity and sensitivity of reconsolidation settlement to the finer characteristics of earthquake ground motions, and would not have yielded the differences in settlement computed herein. Similar to the simulations using RS motions, the maximum r_u at the end of shaking occurred near the surface and decreased with depth [Figs. 16(b) and 17(b)]. In contrast to the RS motions, a greater degree of excess pore-pressure dissipation during shaking was found for the recorded earthquake motions, which led to lower r_u values at the time at which shaking ended and reconsolidation began (Fig. 18). This resulted in reductions in the simulated settlements, because PM4Sand is not able to model settlements that would be expected due to excess pore-pressure dissipation during shaking in a physical system (Ramirez et al. 2018). Values of γ were relatively small and were distributed across the model for Motion M5, whereas they localized near the base of the liquefiable sand for the lower-intensity Motion M1 (with PGA scaled to 0.25g), and at a depth of approximately 7 m for M1 scaled to the higher PGA intensity of 0.53g [Figs. 16(c and c)]. These depths are characterized by relatively low q_{c1Ncs} values (Fig. 3). Values of ε_v were largest near the base of the liquefiable layer [Figs. 16(d) and 17(d)], as was observed with the RS motions with higher PGAs, due to a base-isolation effect caused by liquefaction of the region above, reducing the demands at the shallower depths. Overall, the trends

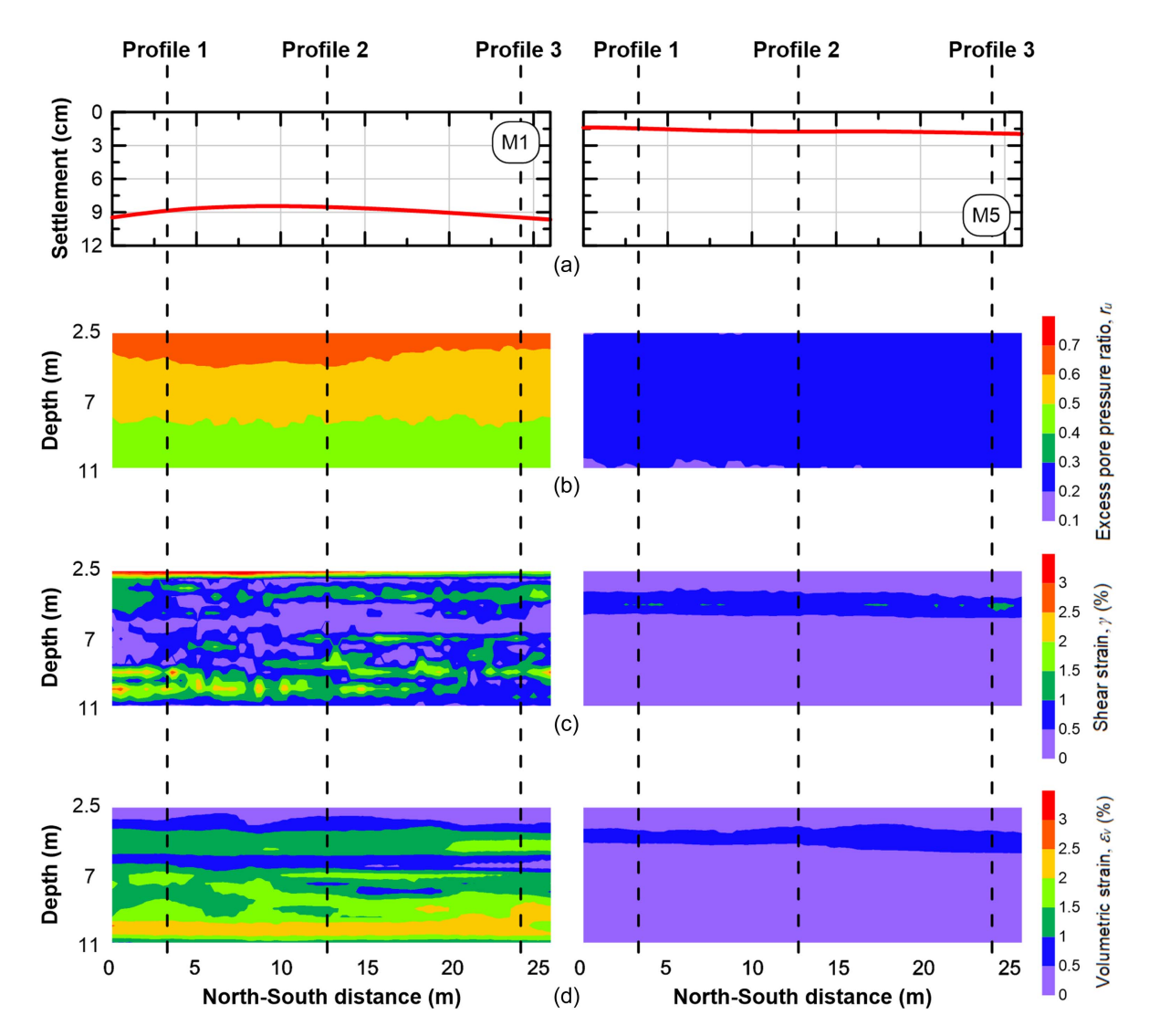


Fig. 16. Responses from simulations of the stochastic soil Section 12 using the recorded earthquake motions M1 and M5: (a) settlement; (b) end-of-shaking r_u ; (c) end-of-shaking γ ; and (d) postreconsolidation ε_v . Both simulations used a PGA of 0.25g.

from the recorded earthquake motions were similar to those observed from the RS motions for this section.

Simulations were repeated for stochastic Sections 1, 5, and 8 using the recorded earthquake motions. The mean settlements from the recorded motions were similar for all four sections, and all were less than the RS motions for similar PGAs [Figs. 19(a and b)], but this was expected because the I_a value of the most intense recorded earthquake motion (M1 with PGA = 0.53g) was similar to the RS motion with PGA = 0.6g. In contrast, the I_a values of the other six recorded motions with PGA = 0.53g were less than half of those for M1. Moreover, some excess pore-pressure dissipation was observed in case of the recorded earthquake motion simulations, a factor that likely led to reduced settlements because the PM4Sand does not model reconsolidation settlements during shaking. Simulations also were conducted using a uniform model with the median q_{c1Ncs} value [Figs. 19(a and b)] for comparison with the stochastic simulations. The mean settlements from the stochastic simulations were nearly identical to that obtained from the uniform model for all motions. Goodness-of-fit statistics such as the coefficient of determination (R^2) , mean squared error (MSE), mean bias (calculated as the ratio of settlement from stochastic and uniform models), and COV (bias) are summarized in Table 3. The median q_{c1Ncs} appears to serve as an excellent predictor of the mean stochastic settlement for the lower PGA, and is slightly conservative for the higher PGA, similar to observations drawn from the RS motions.

The maximum differential settlements from the various sections had significant variation for any particular motion [Fig. 19(c)]. The level of variation was similar to that of the RS motions, but the magnitude of maximum differential settlement as a percent of the mean settlement was larger for the recorded earthquake motions; it varied from 3.5% to 51.3% among the four sections at a PGA of 0.25g, and from 3.3% to 36% at a PGA of 0.53g. These results show that RS motions can give reasonable estimates of liquefaction-induced settlements, although the variability is significantly lower as a result of the uniform motion frequency and duration. Uniform sections with median properties provided reasonable estimates of the mean settlement for all of the stochastic simulations, but cannot provide estimates of differential settlement, which often is more damaging to infrastructure (Polshin and Tokar 1957; Stuedlein et al. 2022).

Discussion

For a soil section with spatially variable properties, as is the case for any real soil deposit, numerical estimation of the liquefaction-induced

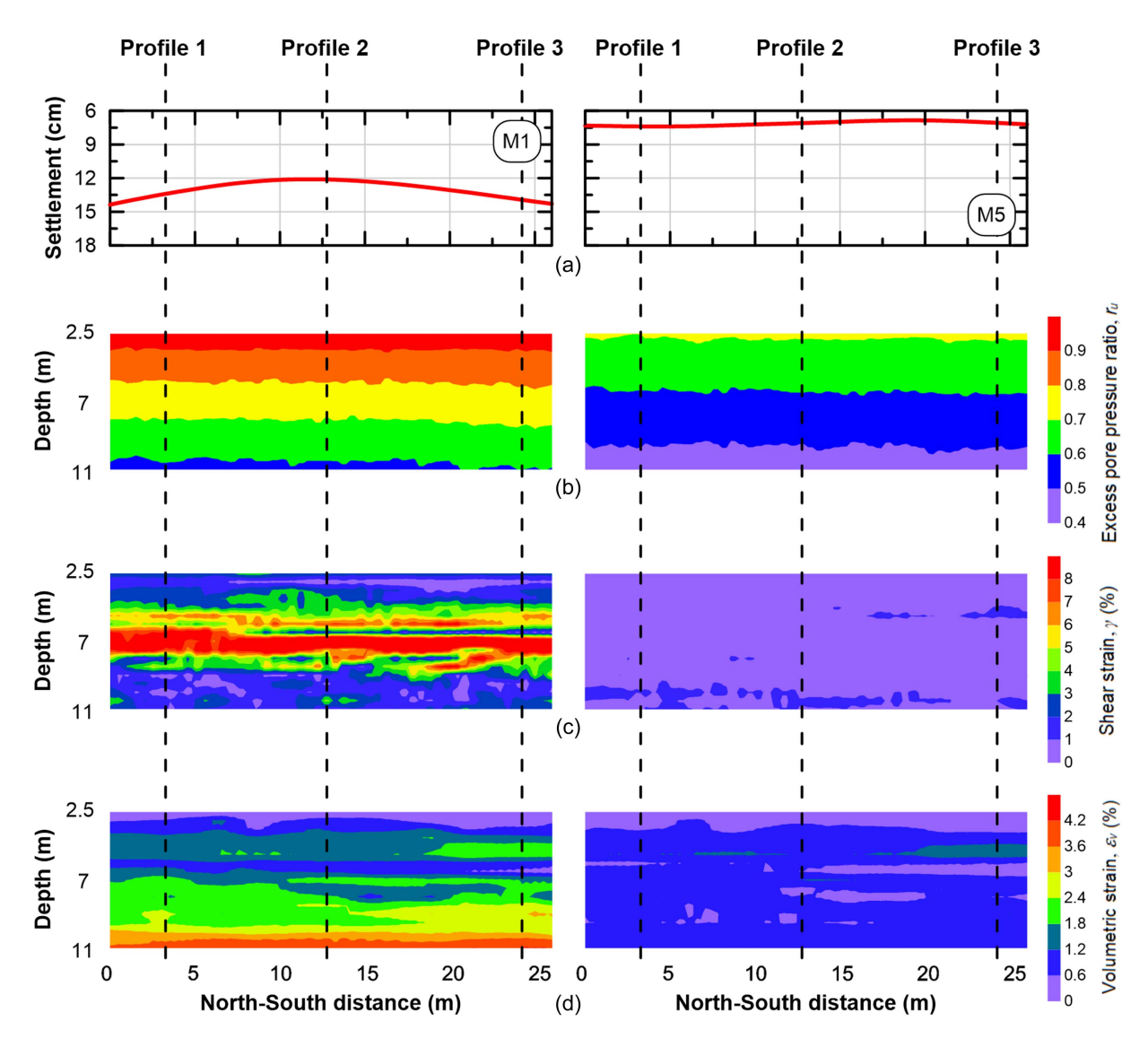


Fig. 17. Responses from simulations of the stochastic soil Section 12 using the recorded earthquake motions M1 and M5: (a) settlement; (b) end-of-shaking r_u ; (c) end-of-shaking γ ; and (d) postreconsolidation ε_v . Both simulations used a PGA of 0.53g.

reconsolidation settlements involves two components: the mean, and the differential settlements. Most experimental and numerical studies assuming a single representative value of relative density or penetration resistance for a soil section can capture the mean settlement, but fail to capture the differential settlement, which often is more detrimental to infrastructure. This study demonstrated that simulations performed considering uniform sections that utilize the median q_{c1Ncs} from a stochastic soil section can estimate the corresponding stochastic mean settlement reasonably well for RS and recorded earthquake motions with a wide range of PGAs. The agreement was excellent at low PGAs and slightly conservative at higher PGAs, which aligns with observations by Montgomery and Boulanger (2017).

However, the maximum differential settlement, calculated as the difference between the maximum and minimum settlements obtained from the ROI of a stochastic section can be captured only by taking into account the stochastic distribution of soil properties within the section. In the case of simulations using RS motions, the maximum differential settlement as a percentage of the mean settlement varied from 5.3% to 8.6% for low PGAs (~0.13g), from 10% to 20.8% for intermediate PGAs (~0.45g), and from 8.4%

to 17% at large PGAs (\sim 0.7g). The simulations using recorded earthquake motions had mean normalized maximum differential settlements ranging from 3.5% to 51.3% for a low PGA (0.25g) and from 3.3% to 36% for a high PGA (0.53g). These observations are consistent with those of Bong and Stuedlein (2018), who they utilized the Yoshimine et al. (2006) empirical framework to compute ε_v and found smaller maximum differential settlements when PGAs were high. These observations indicate that maximum differential settlement as a proportion of the mean settlement may be critical for low-intensity motions, and that accounting for differential settlement hazards using stochastic simulations may be necessary. The continuum model used herein could not capture ejecta, so this observation is limited to cases in which ejecta do not occur, for example, due to a relatively thick surface crust layer.

Selection of the most appropriate lateral boundary conditions in numerical simulations appears to be critical for liquefaction studies. Free-field lateral boundaries have been observed to replicate the in situ condition reasonably well (Chian et al. 2014; Pretell et al. 2022), and were used in this study. A sensitivity analysis appears to be critical for optimization of the distance of the free-field boundaries from the ROI to isolate the ROI from the effects of any

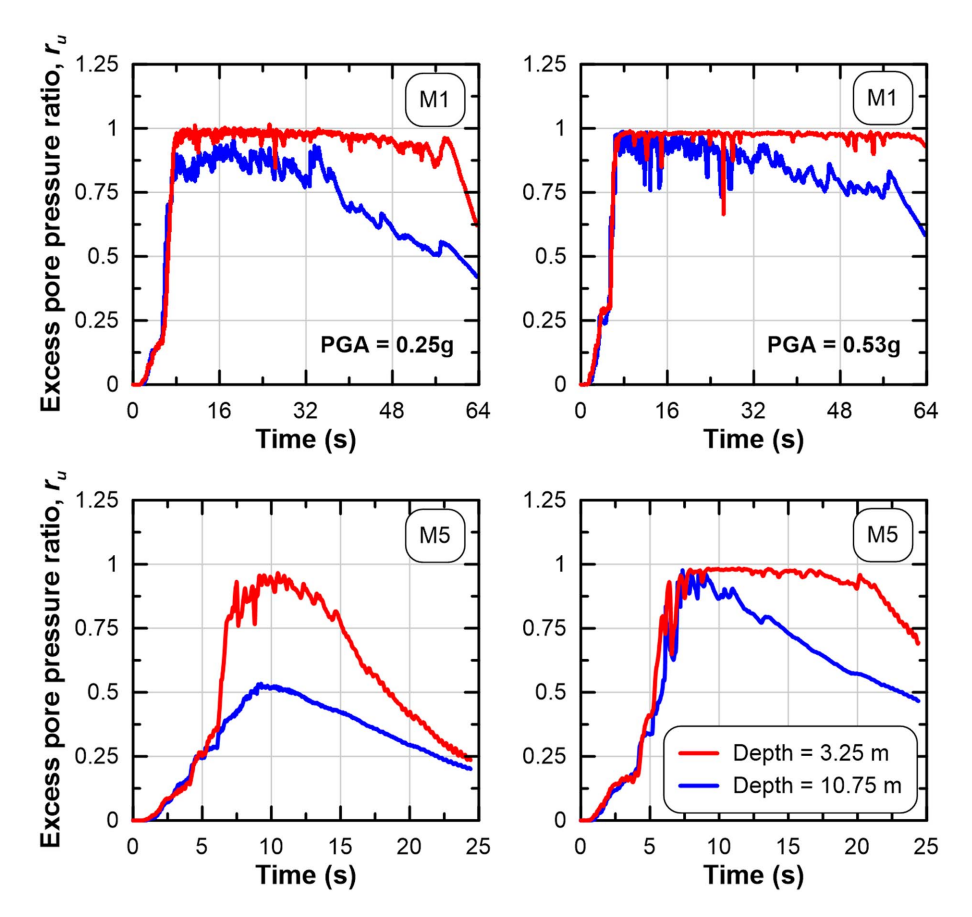


Fig. 18. Time histories of r_u obtained from the simulations corresponding to soil Section 12 using the recorded earthquake motions M1 and M5 at two PGA levels.

numerical artifacts of the free-field boundaries (Chian et al. 2014; Pretell et al. 2022). In this study, a separation distance of 78 m was found to be optimal, beyond which convergence of responses was observed. At smaller separation distances, the boundaries led to much larger maximum differential settlements. The use of attached or periodic boundaries is appropriate for infinite-slope simulations, but was found to lead to more-uniform γ values across the model (due to tied degrees of freedom on each side). This increased the mean settlement and reduced the maximum differential settlement regardless of the separation distance. This result shows that periodic boundaries are not appropriate for level-ground simulations.

The soil-specific calibration of the PM4Sand reconsolidation parameter $f_{\text{sed,min}}$ also is essential for accurate estimation of the magnitudes of reconsolidation settlements (Basu et al. 2022a, 2023). The calibration could be performed either using postliquefaction soil stiffness data, if available, or using experimental or in situ estimates of settlement for the same soil type. Herein, $f_{\rm sed,min}$ was modified from the default PM4Sand value by adjusting it to match the mean settlement observed from a blast-induced liquefaction study conducted at the site (Gianella and Stuedlein 2017). Owing to the multidirectional nature of blast-induced motions (Jana and Stuedlein 2021, 2022; Jana et al. 2023), the calibration of $f_{\rm sed,min}$ indirectly incorporated the effects of multidirectional shaking on reconsolidation settlement (Pyke et al. 1975) despite the use of unidirectional ground motion input. Consideration of multidirectional shaking in forward analyses should evaluate the potential for multidirectional shaking to increase settlements.

This study used 2D soil sections to estimate mean and maximum differential settlements across individual sections stacked at a certain distance interval along the into-the-plane direction. However, to estimate the overall variation in settlements over an area, a 3D numerical modeling of the site is necessary, which was not explored herein. Moreover, the use of harmonic motions at other predominant frequencies and a larger set of recorded earthquake motions to evaluate liquefaction-induced settlements are other aspects that need to be examined in the future. Finally, the reconsolidation modeling approach used in this study used a phenomenological adjustment to the postshaking properties to capture reconsolidation strains. Development of modeling approaches that can directly model effects such as sedimentation and ejecta are needed.

Conclusions

This study investigated the liquefaction-induced mean and maximum differential settlements, along with other postliquefaction responses such as excess pore-pressure ratios (r_u) , shear strains (γ) , and volumetric strains (ε_v) for a well-characterized site at Hollywood, South Carolina. A total of 13 2D stochastic soil sections with a width of 26 m and thickness of 14 m (referred to as the region of interest) from this site were simulated numerically using the numerical platform FLAC and the constitutive model PM4Sand. Free-field lateral boundaries were used at an optimum separation distance from the ROI as estimated through sensitivity analysis. The soil-specific calibration of the PM4Sand reconsolidation parameter $f_{\rm sed,min}$ was performed for accurate prediction of postliquefaction responses. The numerical simulations incorporated spatially variable soil properties such as relative density (D_r) and shear

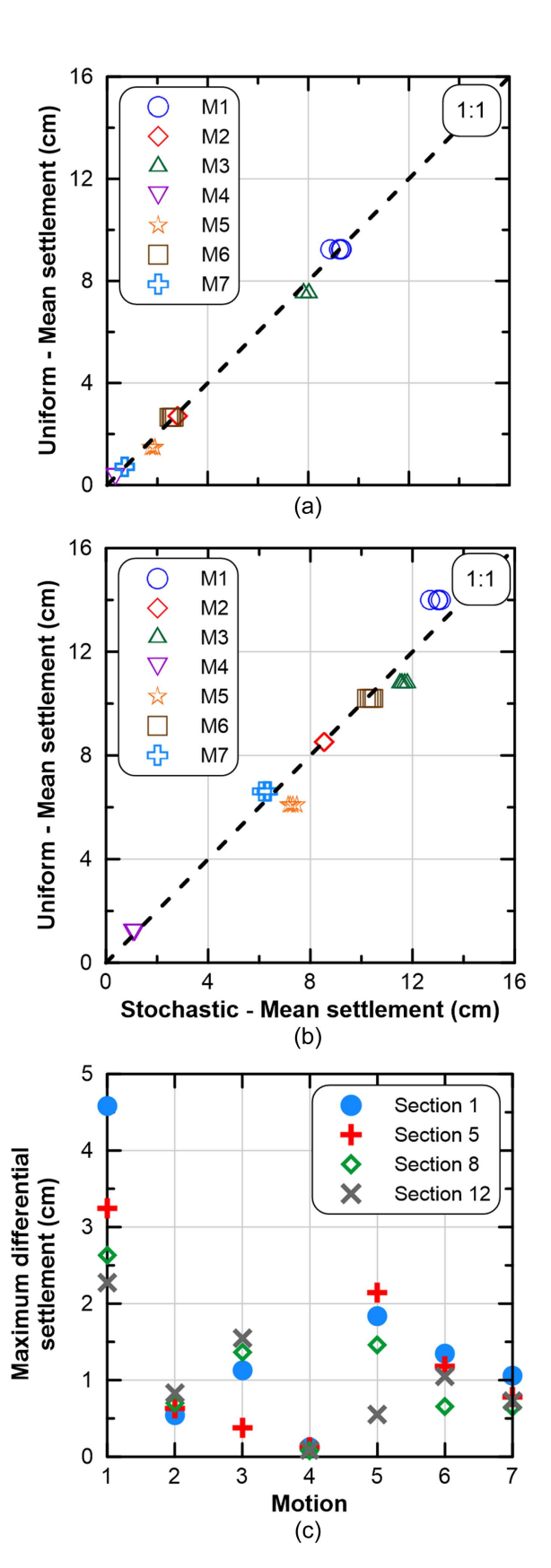


Fig. 19. (a) Simulated mean reconsolidation settlements from four stochastic sections and the uniform section using the representative median q_{c1Ncs} for PGA of 0.25g; (b) simulated mean reconsolidation settlements from four stochastic sections and the uniform section using the representative median q_{c1Ncs} for PGA of 0.53g; and (c) corresponding maximum differential settlements for the recorded earthquake motion suite with PGA = 0.53g.

Table 3. Statistical parameters corresponding to numerical fit of simulated mean settlements from stochastic Section 12 using uniform model assuming representative median q_{c1Ncs}

Parameter	PGA = 0.25g	PGA = 0.53g		
R^2	0.9965	0.9699		
MSE	1.029	1.04		
Mean bias	1.012	1.016		
COV (bias)	0.07	0.084		

Note: All simulations utilized recorded earthquake motion suite.

modulus based on correlations with the measured clean sand-corrected cone tip resistance (q_{c1Ncs}). A few representative uniform soil sections using median and percentile values from the q_{c1Ncs} distribution for the stochastic deposit were subjected to shaking to determine their ability to estimate reconsolidation settlements compared with those from the stochastic model. Ramped sinusoidal input motions with different peak ground accelerations and a suite of recorded earthquake motions linearly-scaled to two PGAs (0.25 and 0.53g) that corresponded to the expected hazard at the Hollywood site were applied to the base of the soil model.

Some of the key observations from this study include the following:

- The soil-specific calibration of the PM4Sand reconsolidation parameter f_{sed,min} was critical for accurate prediction of reconsolidation settlements. The default PM4Sand parameter f_{sed,min} was modified by adjusting it to match the mean reconsolidation settlement observed following a blast-induced liquefaction experiment of the deposit simulated herein and by using the correlation developed by Basu et al. (2022a) based on centrifuge tests on clean sands. The soil-specific calibration fell between the default values and that resulting from the correlation suggested by Basu et al. (2022a).
- Higher r_u values were observed at shallower depths in stochastic sections with the thickness of the zone of initial liquefaction increasing with an increase in PGA for the case of RS motions and with an increase in CAV and I_a for the recorded earthquake motions. Lateral variation of r_u was found to be insignificant in any of the simulations, due to possible redistribution of pore pressures in the lateral direction.
- The distribution of γ was found to be dependent on both the q_{c1Ncs} distribution of a given soil section and the r_u distribution following liquefaction. The magnitude of γ depended on the evolutionary intensity measures such as CAV and I_a . The shear strain localized in regions of lower q_{c1Ncs} and higher r_u , but as soon as initial liquefaction ($r_u \approx 1$) conditions developed, a reduction in the demand above the liquefied area was observed due to damping of seismic energy at these depths, even if these zones had low q_{c1Ncs} .
- ε_v was found to be concentrated in zones that corresponded to low q_{c1Ncs} values. They also were found to attenuate for intermediate PGAs (\sim 0.45g), leading to an asymptotic mean settlement relationship.
- For any particular motion, the mean settlements derived from the stochastic sections were similar; however, considerable variation in maximum differential settlements among the sections was found owing to differences in the lateral distribution of q_{c1Ncs} .
- Uniform models using the median properties from the stochastic sections were able to predict the mean settlements reasonably well. However, the inherent limitation of uniform models lies in their inability to predict differential settlements, which often are responsible for the majority of damage to infrastructure.

- The stochastic simulations performed herein highlighted that the maximum differential settlement for a section can be a significant percentage of its mean settlement (exceeding 50%). Critically, the mean normalized maximum differential settlements were found to be higher at lower PGAs.
- One-dimensional empirical modeling approaches overestimated both the mean and maximum differential settlement compared with the numerical models. This is attributed to three factors: redistribution of excess pore pressures between loose and dense zones; the two dimensional strain patterns observed in the simulations, which tended to concentrate in weaker bands; and the inability of the empirical approaches to capture reductions in loading on shallower layers as deeper zones liquefy. These factors would be difficult if not impossible to include in a simplified model, which highlights one of the advantages of using numerical models.

Data Availability Statement

Some or all data, models, or code that support the findings of this study are available from the corresponding author upon reasonable request.

Acknowledgments

The first author is grateful for the financial support provided by the Department of Civil and Environmental Engineering at Auburn University. The third author was funded over the course of this work by the National Science Foundation (NSF) under Grant CMMI 1931069. The findings presented herein are those of the authors, and do not necessarily represent views of NSF.

Supplemental Materials

Figs. S1–S3 are available online in the ASCE Library (www.ascelibrary.org).

References

- Andrus, R. D., R. Boller, W. M. Camp, S. Gassman, M. Hasek, H. Hayati, and P. Talwani. 2008. "Characterizing the liquefaction resistance of aged soils: Summary of selected first year findings." In *Proc.*, *NSF* Engineering Research and Innovation Conf. Alexandria, VA: National Science Foundation CMMI.
- Arulanandan, K., and J. J. Sybico. 1992. "Post-liquefaction settlement of sand." In *Proc.*, Wroth Memorial Symp. London: T. Telford.
- Baker, J. W., T. Lin, S. K. Shahi, and N. Jayaram. 2011. New ground motion selection procedures and selected motions for the PEER transportation research program. PEER Rep. Berkeley, CA: Univ. of California.
- Banister, J. R., L. Winters, D. M. Ellett, and R. M. Pyke. 1976. "In-situ pore presure measurements at Rio Blanco." *J. Geotech. Eng. Div.* 102 (10): 1073–1091. https://doi.org/10.1061/AJGEB6.0000332.
- Basu, D., J. Montgomery, and A. W. Stuedlein. 2022a. "Observations and challenges in simulating post-liquefaction settlements from centrifuge and shake table tests." Soil Dyn. Earthquake Eng. 153 (May): 107089. https://doi.org/10.1016/j.soildyn.2021.107089.
- Basu, D., J. Montgomery, and A. W. Stuedlein. 2023. "Uncertainty in liquefaction-induced settlement in numerical simulations due to model calibration." In *Proc.*, *Geo-Risk*. Reston, VA: ASCE.
- Basu, D., R. Pretell, J. Montgomery, and K. Ziotopoulou. 2022b. "Investigation of key parameters and issues in simulating centrifuge model tests of a sheet-pile wall retaining a liquefiable soil deposit." Soil

- *Dyn. Earthquake Eng.* 156 (May): 107243. https://doi.org/10.1016/j.soildyn.2022.107243.
- Beyzaei, C. Z., J. D. Bray, M. Cubrinovski, S. Bastin, M. Stringer, M. Jacka, S. van Ballegooy, M. Riemer, and R. Wentz. 2020. "Characterization of silty soil thin layering and groundwater conditions for lique-faction assessment." *Can. Geotech. J.* 57 (2): 263–276. https://doi.org/10.1139/cgj-2018-0287.
- Bong, T., and A. W. Stuedlein. 2017. "Spatial variability of CPT parameters and silty fines in liquefiable beach sands." J. Geotech. Geoenviron. Eng. 143 (12): 04017093. https://doi.org/10.1061/(ASCE)GT.1943-5606 0001789
- Bong, T., and A. W. Stuedlein. 2018. "Effect of cone penetration conditioning on random field model parameters and impact of spatial variability on liquefaction-induced differential settlements." J. Geotech. Geoenviron. Eng. 144 (5): 04018018. https://doi.org/10.1061/(ASCE)GT.1943-5606.0001863.
- Boulanger, R., and K. Ziotopoulou. 2017. *PM4Sand (Version 3.1): A sand plasticity model for earthquake engineering applications*. Rep. No. UCD/CGM-17/01, Davis, CA: Univ. of California, Davis.
- Boulanger, R. W., and I. M. Idriss. 2016. "CPT-Based liquefaction triggering procedure." J. Geotech. Geoenviron. Eng. 142 (2): 04015065. https://doi.org/10.1061/(ASCE)GT.1943-5606.0001388.
- Bwambale, B., and R. D. Andrus. 2019. "State of the art in the assessment of aging effects on soil liquefaction." *Soil Dyn. Earthquake Eng.* 125 (Mar): 105658. https://doi.org/10.1016/j.soildyn.2019.04.032.
- Cary, J. R., A. W. Stuedlein, C. R. McGann, B. A. Bradley, and B. W. Maurer. 2022. "Effect of refinements to CPT-based liquefaction triggering analysis on liquefaction severity indices at the Avondale playground site, Christchurch, NZ." In Proc., 4th Int. Conf. on Performance Based Design in Earthquake Geotechnical Engineering, 1454–1466. Berlin: Springer.
- Chen, Q., C. Wang, and C. H. Juang. 2016. "Probabilistic and spatial assessment of liquefaction-induced settlements through multiscale random field models." *Eng. Geol.* 211: 135–149. https://doi.org/10.1016/j.enggeo.2016.07.002.
- Chian, S. C., K. Tokimatsu, and S. P. G. Madabhushi. 2014. "Soil liquefaction-induced uplift of underground structures: Physical and numerical modeling" *J. Geotech. Geoenviron. Eng.* 140 (10): 04014057. https://doi.org/10.1061/(ASCE)GT.1943-5606.0001159.
- Cubrinovski, M., A. Rhodes, N. Ntritsos, and S. Van Ballegooy. 2019. "System response of liquefiable deposits" *Soil Dyn. Earthquake Eng.* 124 (Feb): 212–229. https://doi.org/10.1016/j.soildyn.2018.05.013.
- Dafalias, Y. F., and M. T. Manzari. 2004. "Simple plasticity sand model accounting for fabric change effects" *J. Eng. Mech.* 130 (6): 622–634. https://doi.org/10.1061/(ASCE)0733-9399(2004)130:6(622).
- DeGroot, D. J., and G. B. Baecher. 1993. "Estimating autocovariance of in-situ soil properties" *J. Geotech. Eng.* 119 (1): 147–166. https://doi.org/10.1061/(ASCE)0733-9410(1993)119:1(147).
- Doar, R. D., III, and C. G. St. C. Kendall. 2014. "An analysis and comparison of observed Pleistocene South Carolina (USA) shoreline elevations with predicted elevations derived from marine oxygen isotope stages" Q. Res. 82 (Feb): 164–174. https://doi.org/10.1016/j.yqres.2014.04.005.
- Fenton, G. A., and E. H. Vanmarcke. 1998. "Spatial variation in liquefaction risk." *Géotechnique* 48 (6): 819–831. https://doi.org/10.1680/geot.1998.48.6.819.
- Geyin, M., and B. W. Maurer. 2019. "An analysis of liquefaction-induced free-field ground settlement using 1,000+ case histories: Observations vs. state-of-practice predictions." In *Proc., Geo-Congress*, 489–498. Reston, VA: ASCE.
- Gianella, T. N. 2015. "Ground improvement and liquefaction mitigation using driven timber piles." Master thesis, Dept. of Civil and Construction Engineering, Oregon State Univ.
- Gianella, T. N., and A. W. Stuedlein. 2017. "Performance of driven displacement pile-improved ground in controlled blasting field tests." J. Geotech. Geoenviron. Eng. 143 (9): 04017047. https://doi.org/10.1061/(ASCE)GT.1943-5606.0001731.
- Green, R. A., B. W. Maurer, and S. V. Ballegooy. 2018. "The influence of the non-liquefied crust on the severity of surficial liquefaction manifestations: Case history from the 2016 valentine's day earthquake in

- New Zealand." In Geotechnical earthquake engineering and soil dynamics V, 21–32. Reston, VA: ASCE.
- Griffiths, D. V., G. A. Fenton, and N. Manoharan. 2002. "Bearing capacity of rough rigid strip footing on cohesive soil: Probabilistic study." *J. Geotech. Geoenviron. Eng.* 128 (9): 743–755. https://doi.org/10 .1061/(ASCE)1090-0241(2002)128:9(743).
- Howell, R., E. Rathje, and R. Boulanger. 2015. "Evaluation of simulation models of lateral spread sites treated with prefabricated vertical drains." *J. Geotech. Geoenviron. Eng.* 141 (1): 04014076. https://doi.org/10.1061/(ASCE)GT.1943-5606.0001185.
- Idriss, I. M., and R. W. Boulanger. 2008. Soil liquefaction during earth-quakes. Monograph MNO-12. Oakland, CA: Earthquake Engineering Research Institute.
- Ishihara, K., and M. Yoshimine. 1992. "Evaluation of settlements in sand deposits following liquefaction during earthquakes." Soils Found. 32 (1): 173–188. https://doi.org/10.3208/sandf1972.32.173.
- Itasca. 2016. FLAC (Version 8.0)—Fast Lagrangian analysis of continua. Reston, VA: Itasca Consulting Group.
- Jafarzadeh, F., and E. Yanagisawa. 1995. "Settlement of sand models under unidirectional shaking." In Proc., First Int. Conf. on Earthquake Geotechnical Engineering, 693–698. Reston, VA: ASCE.
- Jana, A., A. Dadashiserej, B. Zhang, A. W. Stuedlein, T. M. Evans, K. H. Stokoe, II, and B. R. Cox. 2023. "Multidirectional vibroseis shaking and controlled blasting to determine the dynamic in situ response of a low-plasticity silt deposit." *J. Geotech. Geoenviron. Eng.* 149 (3): 04023006. https://doi.org/10.1061/(ASCE)GT.1943-5606.0002924.
- Jana, A., and A. W. Stuedlein. 2021. "Dynamic in situ nonlinear inelastic response of a deep medium dense sand deposit." J. Geotech. Geoenviron. Eng. 147 (6): 04021039. https://doi.org/10.1061/(ASCE)GT .1943-5606.0002523.
- Jana, A., and A. W. Stuedlein. 2022. "Dynamic, in situ, nonlinear-inelastic response and post-cyclic strength of a plastic silt deposit." *Can. Geo*tech. J. 59 (1): 111–128. https://doi.org/10.1139/cgj-2020-0652.
- Kuhlemeyer, R. L., and J. Lysmer. 1973. "Finite element method accuracy for wave propagation problems." J. Soil Mech. Found. Div. 99 (5): 421–427. https://doi.org/10.1061/JSFEAQ.0001885.
- Lewis, M. R., I. Arango, and M. D. McHood. 2008. "Site characterization philosophy and liquefaction evaluation of aged sands—A Savannah River Site and Bechtel perspective." In *From research to practice in* geotechnical engineering, 540–558. Aachen, Germany: Deutsche Ges. fur Erd- und Grundbau.
- Lumb, P. 1975. "Spatial variability of soil properties." In Proc., 2nd Int. Conf. on Application of Statistics and Probability in Soil and Structural Engineering, 397–421. Reston, VA: ASCE.
- Mahvelati, S., J. T. Coe, A. W. Stuedlein, P. Asabere, and T. N. Gianella. 2016. "Time-rate variation of the shear wave velocity (site stiffness) following blast-induced liquefaction." In *Proc.*, *Geo-Chicago GSP* 271. Reston, VA: ASCE.
- Mahvelati, S., J. T. Coe, A. W. Stuedlein, P. Asabere, T. N. Gianella, and A. Kordjazi. 2020. "Recovery of small-strain stiffness following blast-induced liquefaction based on shear wave velocity measurements." Can. Geotech. J. 58 (6): 848–865. https://doi.org/10.1139 /cgj-2019-0658.
- Malvick, E. J., B. L. Kutter, R. W. Boulanger, and R. Kulasingam. 2006. "Shear localization due to liquefaction-induced void redistribution in a layered infinite slope." *J. Geotech. Geoenviron. Eng.* 132 (10): 1293–1303. https://doi.org/10.1061/(ASCE)1090-0241(2006)132:10(1293).
- Maybin, G. R., and P. G. Nystrom. 1997. Geologic and resource map of South CarolinaSC Geological Survey. Clemson, SC: South Carolina Geological Survey.
- Mejia, L., and E. Dawson. 2006. "Earthquake deconvolution for FLAC." In Proc., 4th Int. FLAC Symp. on Numerical Modeling in Geomechanics. Reston, VA: Itasca Consulting Group.
- Montgomery, J., and R. W. Boulanger. 2017. "Effects of spatial variability on liquefaction-induced settlement and lateral spreading." *J. Geotech. Geoenviron. Eng.* 143 (1): 04016086. https://doi.org/10.1061/(ASCE) GT.1943-5606.0001584.
- Nagase, H., and K. Ishihara. 1988. "Liquefaction-induced compaction and settlement of sand during earthquakes." Soils Found. 28 (1): 65–76. https://doi.org/10.3208/sandf1972.28.65.

- Nuttli, O., G. Bollinger, and R. Herrmann. 1986. The 1886 Charleston, South Carolina, earthquake—A 1986 perspective. Reston, VA: USGS.
- Phoon, K.-K., and F. H. Kulhawy. 1999. "Characterization of geotechnical variability." Can. Geotech. J. 36 (4): 612–624. https://doi.org/10.1139 //199-038
- Polshin, D., and R. Tokar. 1957. "Maximum allowable non-uniform settlement of structures." In *Proc.*, 4th ICSMFE, 402–406. London: International Society for Soil Mechanics and Geotechnical Engineering.
- Popescu, R., J. H. Prevost, and G. Deodatis. 1997. "Effects of spatial variability on soil liquefaction: Some design recommendations." *Géotechnique* 47 (5): 1019–1036. https://doi.org/10.1680/geot.1997.47.5.1019.
- Pretell, R., K. Ziotopoulou, and N. A. Abrahamson. 2022. "Conducting 1D site response analyses to capture 2D V_S spatial variability effects." *Earthquake Spectra* 38 (3): 2235. https://doi.org/10.1177/8755293021 1069400.
- Pyke, R. M., C. K. Chan, and H. B. Seed. 1975. "Settlement of sands under multidirectional shaking." J. Geotech. Eng. Div. 101 (4): 379–398. https://doi.org/10.1061/AJGEB6.0000162.
- Ramirez, J., A. R. Barrero, L. Chen, S. Dashti, A. Ghofrani, M. Taiebat, and P. Arduino. 2018. "Site response in a layered liquefiable deposit: Evaluation of different numerical tools and methodologies with centrifuge experimental results." *J. Geotech. Geoenviron. Eng.* 144 (10): 04018073. https://doi.org/10.1061/(ASCE)GT.1943-5606.0001947.
- Rauthause, M. P., A. W. Stuedlein, and M. J. Olsen. 2020. "Quantification of surface roughness using laser scanning with application to the frictional resistance of sand-timber pile interfaces." *Geotech. Test. J.* 43 (4): 20180384. https://doi.org/10.1520/GTJ20180384.
- Robertson, P. K., and C. E. Wride. 1998. "Evaluating cyclic liquefaction potential using the cone penetration test." *Can. Geotech. J.* 35 (5): 442–459. https://doi.org/10.1139/t98-017.
- Seed, H. B., and K. L. Lee. 1966. "Liquefaction of saturated sands during cyclic loading." J. Soil Mech. Found. Div. 92 (6): 105–134. https://doi .org/10.1061/JSFEAQ.0000913.
- Sento, N., M. Kazama, and R. Uzuoka. 2004. "Experiment and idealization of the volumetric compression characteristics of clean sand after undrained cyclic shear." [In Japanese.] *Doboku Gakkai Ronbunshu* 2004 (764): 307–317. https://doi.org/10.2208/jscej.2004.764_307.
- Shahir, H., A. Pak, M. Taiebat, and B. Jeremić. 2012. "Evaluation of variation of permeability in liquefiable soil under earthquake loading." *Comput. Geotech.* 40 (Mar): 74–88. https://doi.org/10.1016/j.compgeo.2011.10.003.
- Stuedlein, A., and T. N. Gianella. 2016. *Drained timber pile ground im*provement for liquefaction mitigation. NCHRP IDEA project Rep. 180. Washington, DC: NCHRP IDEA Program.
- Stuedlein, A. W., and T. Bong. 2017. "Effect of spatial variability on static and liquefaction-induced differential settlements." In *Proc.*, *Geo-Risk* GSP 282. Reston, VA: ASCE.
- Stuedlein, A. W., T. Bong, J. Montgomery, J. Ching, and K. K. Phoon. 2021. "Effect of densification on the random field model parameters of liquefiable soil and their use in estimating spatially-distributed liquefaction-induced settlement." *Int. J. Geoeng. Case Histories* 6 (4): 17. https://doi.org/10.4417/IJGCH-06-04-01.
- Stuedlein, A. W., T. N. Gianella, and G. Canivan. 2016. "Densification of granular soils using conventional and drained timber displacement piles." *J. Geotech. Geoenviron. Eng.* 142 (12): 04016075. https://doi.org/10.1061/(ASCE)GT.1943-5606.0001554.
- Stuedlein, A. W., J. C. Huffman, A. R. Barbosa, and A. F. Belejo. 2022. "Probabilistic structural system response to differential settlement resulting from spatially variable soil." J. Geotech. Geoenviron. Eng. 148 (2): 04021184. https://doi.org/10.1061/(ASCE)GT .1943-5606.0002735.
- Stuedlein, A. W., A. Jana, A. Dadashiserej, and X. Yang. 2023. "On the in situ cyclic resistance of natural sand and silt deposits." *J. Geotech. Geoenviron. Eng.* 149 (4): 04023015. https://doi.org/10.1061/JGGEFK .GTENG-10784.
- Tokimatsu, K., and H. B. Seed. 1987. "Evaluation of settlements in sands due to earthquake shaking." *J. Geotech. Eng.* 113 (8): 861–878. https://doi.org/10.1061/(ASCE)0733-9410(1987)113:8(861).
- USGS. 2014. Unified hazard tool. Reston, VA: USGS.

- Vanmarcke, E. H. 1977. "Probabilistic modeling of soil profiles." J. Geotech. Eng. Div. 103 (11): 1227–1246. https://doi.org/10.1061/AJGEB6.0000517.
- Yoshimine, M., H. Nishizaki, K. Amano, and Y. Hosono. 2006. "Flow deformation of liquefied sand under constant shear load and its application to analysis of flow slide of infinite slope." Soil Dyn. Earthquake Eng. 26 (2–4): 253–264. https://doi.org/10.1016/j.soildyn .2005.02.016.
- Yost, K. M., B. R. Cox, L. Wotherspoon, R. W. Boulanger, S. van Ballegooy, and M. Cubrinovski. 2019. "In situ investigation of
- false-positive liquefaction sites in Christchurch, New Zealand: Palinurus Road case history." In *Proc., Geo-Congress*, 436–451. Reston, VA: ASCE.
- Youd, T. L., and C. T. Garris. 1995. "Liquefaction-induced ground-surface disruption." J. Geotech. Eng. 121 (11): 805–809. https://doi.org/10 .1061/(ASCE)0733-9410(1995)121:11(805).
- Ziotopoulou, K., and R. W. Boulanger. 2013. "Numerical modeling issues in predicting post-liquefaction reconsolidation strains and settlements." In *Proc., 10th Int. Conf. on Urban Earthquake Engineering*, 1–2. Tokyo: Center for Urban Earthquake Engineering.